THE EFFECTS OF CULTURAL NOISE ON CONTROLLED SOURCE ELECTROMAGNETIC RESPONSES OF SUBSURFACE FRACTURES IN RESISTIVE TERRAIN

A Thesis

by

ROLAND ANTHONY SAVIO FERNANDES

Submitted to the Office of Graduate Studies of
Texas A&M University
in partial fulfillment of the requirements for the degree of

MASTER OF SCIENCE

May 2008

Major Subject: Geophysics

THE EFFECTS OF CULTURAL NOISE ON CONTROLLED SOURCE ELECTROMAGNETIC RESPONSES OF SUBSURFACE FRACTURES IN RESISTIVE TERRAIN

A Thesis

by

ROLAND ANTHONY SAVIO FERNANDES

Submitted to the Office of Graduate Studies of
Texas A&M University
in partial fulfillment of the requirements for the degree of

MASTER OF SCIENCE

Approved by:

Chair of Committee,	Mark Everett
Committee Members,	Hongbin Zhan
	Clyde Munster
Head of Department,	Andreas Kronenberg

May 2008

Major Subject: Geophysics

ABSTRACT

The Effects of Cultural Noise on Controlled Source Electromagnetic Responses of Subsurface Fractures in Resistive Terrain.

(May 2008)

Roland Anthony Savio Fernandes, B.S., University of Mumbai; M.S., University of Pune

Chair of Advisory Committee: Dr. Mark Everett

Controlled source electromagnetic (CSEM) geophysics has been used with a fair amount of success in near surface hydrogeological studies. Recently, these investigations have been conducted frequently in human impacted field sites containing cultural conductors such as metal fences and buried pipes. Cultural noise adds an element of complexity to the geological interpretation of this type of data. This research investigates the influence of mutual induction between two buried targets in a CSEM experiment. In particular, it looks at the mutual coupling between a buried cultural conductor and a geological heterogeneity. We attempt to isolate the H_z field induced by tertiary currents in targets caused by mutual coupling. This is achieved with a Texas A&M 3D CSEM finite element code, which calculates the secondary $\mathbf{H}_z$ fields emanating from a target buried in a halfspace. Buried geological targets and cultural conductors are modeled as volumetric slabs embedded in a halfspace. A series of models have been simulated to study the effect of varying parameters such as target conductivity, transmitter location and shape of a target on the mutual inductance. In each case, the secondary $\mathbf{H}_z$ field is calculated for a model with two slabs, and two models with individual slabs. The mutual coupling is calculated by removing the secondary fields from the individual slab models from the response of a two slab model. The calculations of mutual inductance from a variety of such models suggests a complicated interaction of EM fields between the two targets. However, we can explain most of these complexities by adapting a simple approach to Maxwell's equations.

Although the tertiary $\mathbf{H}_z$ field is complicated, it may be useful in the characterization and delineation of electrical heterogeneities in the subsurface, which can then be related to geological features such as fractures or joints. It is seen that the most important factor affecting the mutual coupling is the host conductivity. The results have also shown that mutual coupling is very sensitive to transmitter (TX) location, especially when the TX is positioned near one of the targets.

ACKNOWLEDGEMENTS

First and foremost, I would like to thank my advisor, Dr. Mark Everett for his continued support, encouragement and guidance through my MS degree.

I would also like to thank the other members of my committee, Dr. Hongbin Zhan and Dr. Clyde Munster for their support.

This project would not be possible without the help of Souvik Mukherjee, Doug Sassen, and Kayla Berry.

Finally, thanks to my family, friends and the staff at the coffee shop.

TABLE OF CONTENTS

CHAPTER Page

LIST OF FIGURES

FIGURE Page

FIGURE Page

LIST OF TABLES

CHAPTER I
INTRODUCTION

1.1 Introduction to CSEM

Electromagnetic (EM) geophysics deals with the determination and characterization of electric and/or magnetic heterogeneities in the subsurface. These include anomalies in properties such as conductivity, electrical permittivity, and magnetic permeability which vary with different materials. Conductivity is the ability of a material to sustain a current flow. This depends on the number of free or mobile electrons that can travel in the presence of a voltage potential difference. There are 4 main types of conductors. These are metals, semiconductors, electrolytes and insulators. Typically, metallic material has a higher conductivity than non metallic material. This is because metals have a higher number of free or mobile electrons and can sustain a current better than non metals. In an EM geophysical experiment, the final objective is to relate conductivity to geological media with respect to lithology and structure. This objective is not easily achieved because EM measurements are sensitive to the bulk conductivity averaged over some volume around a given recording point. A detailed analysis of the spatiotemporal variations in the dataset is required to delineate heterogeneities in the subsurface.

EM has been used as a tool for subsurface hydrogeological studies, where it has been fairly successful in determining hydrogeological features such as subsurface conduits that allow flow of groundwater. This may be attributed to the differential conductivity between the hydrogeological feature filled with groundwater and the surrounding host medium. Subsurface hydrogeological variations could arise from a number of sources, such as fractures, bedding planes and erosional features such as subsurface channels and caves. It is important to account for these when modeling EM

This thesis follows the style of Geophysics.

responses for hydrogeological purposes (Fitterman and Labson, 2005). However, it is also important to account for cultural conductors, whose response to EM excitation generally adds an element of noise to the dataset via mutual coupling. This is particularly true when analyzing data from a human impacted field site.

Any geophysical data gathered from a human impacted field site is bound to contain some amount of cultural noise. Cultural noise may be defined as that part of the data which is generated by non geological media, mostly human artifacts such as cables, pipes and railroad tracks. The location of these artifacts could either be known or unknown. This research aims to better understand the effect of cultural noise on geophysical time domain electromagnetic data. In particular, it aims to study the effect of mutual coupling between cultural conductors and resistive natural bodies in the subsurface, wherein an inductive process causes a conductive body to behave like a secondary source for an EM field.

This research undertaken here is important because the ability to isolate and account for cultural noise will greatly improve the interpretation of electromagnetic geophysical data at human impacted sites. Increasingly many practical geophysical imaging problems carried out by industry or environmental consulting firms occur at sites that have substantial amounts of cultural noise. In EM experiments, removal of cultural noise is particularly challenging because of the non linear inductive mutual coupling between cultural conductors and fluid or clay filled fractures. The cultural noise in EM furthermore is coherent or signal-generated noise that cannot be removed by filtering, stacking or other conventional data processing steps.

The motivation for this study stems from previous work at a field site in the Edwards Aquifer, near Boerne, Texas, by the Rangeland Ecology and Agricultural Engineering Depts, Texas A&M University. The prior studies have examined the effects of increased brush population on the water cycle and hydrology of the Edwards Plateau (*Taucer*, 2006). The field site has known sources of cultural noise. For example, a vertical semi-buried aluminum sheet acts as a boundary for the main study area. Rainfall simulation and site flooding experiments have suggested the presence of a zone of

intense infiltration at the site. This zone is suspected to contain fractures, which are likely due to ancient regional tectonic stresses (Ferrill *et al*., 2004). The Edwards Aquifer yields a large amount of water along the Baclones Fault zone (Collins, 1987). Within the Balcones fault zone, normal faults are commonly associated with an adjoining region of highly fractured strata. (Collins, 1995) The lithology at the field site is comprised mainly of the lower Cretaceous Glen Rose limestone, interbedded with thin layers of marlstone and claystone (Mancini and Scott, 2006). Subsurface channeling of acidic groundwater through joints may enlarge such pre-existing fractures. The primary purpose of this geophysical study is to provide characterization of the type of response to be expected from a CSEM experiment conducted in the presence of cultural noise. In order to accomplish this goal, field data were collected from the field site, which has a known source of cultural noise. The effect of the artifacts on the measured EM responses is simulated using a 3D controlled-source electromagnetic (CSEM) finite element code and examined with respect to the possibility of ameliorating the effects of cultural noise.

1.2 Literature review

Controlled source EM (CSEM) techniques have long been used in the mining industry for detection of conductive ore bodies. EM has also been used extensively for petroleum well logging. Other than that its use was traditionally restricted to academics and some hydrogeological studies. Recently however, marine CSEM has become an important tool for hydrocarbon detection in the oil and gas industry. It is important to recognize that the EM prospecting method responds sensitively to the conductivity contrast between the host material and the target in question. EM geophysical methods may also be used for general subsurface mapping based on spatial variations in electrical conductivity. Our interests in this research lie in studying the mutual coupling between a resistive or conductive geological heterogeneity and a conductive cultural target in a hydrogeological setting where naturally occurring fractures may provide a flow-path for groundwater.

There have been some recent efforts directed towards the detection and quality assessment of groundwater and aquifer characterization using EM methods. EM inversion has been for environmental purposes have previously been achieved by Sasaki (2001). Sasaki and Meju (2006) performed a 2.5 D inversion of time-domain EM (TDEM) and frequency -domain EM (FDEM) data to characterize heterogeneity in crystalline granitic terrain in Brazil. The goal of their research was to detect subsurface conduits for groundwater flow. Their forward modeling approach was based on a finite difference method using a 3D staggered grid. In their inversion scheme, they use the regularized 'Occam's Inversion' technique (Constable, et al., 1987) to find the smoothest model that is consistent with the data. They also use a second regularization parameter to account for *a priori* information on the subsurface electrical properties of the region. As a test of the inversion scheme, data were inverted from different field sites in Brazil. A preliminary inspection of data from a site at the Currais fracture zone suggest the presence of a dipping dyke, but a quantitative inversion of these data reveals the presence of a deeper less resistive structure, which has been interpreted as a zone of weathering, which extends to a depth of below 60 m but is confined within fractured or sheared granitic material. This structure would not have been predicted based on a qualitative interpretation of data.

Skinner and Heinson (2004) showed that FDEM methods can be used to characterize subsurface anisotropy and its effects on fluid flow. They assumed that the fractures at their field site provide a good conduit for both fluid and electric charge transport. By measuring the change in amplitude and phase from a small transmitter (TX) loop with a receiver (RX) coil, they characterized the apparent conductivity of the underlying ground. Azimuthal surveys were conducted using the EM 34 (Geonics) equipment and data were represented as Rose diagrams of apparent conductivity. TX-RX separations of 10m, 20m and 40m were used at 30° azimuthal spacing. The orientations of ellipses of apparent conductivity were found to be consistent with the direction of strike of the bedding planes, implying maximum groundwater flow path occurred preferably along the bedding planes.

Collins *et al.* (2006) used azimuthal TDEM to characterize electrical anisotropy in the foliated Packsaddle schist formation in central Texas, within the Llano uplift. Using the time domain Geonics Protem 47 instrument, electrical anisotropy was found to be aligned in the direction of schistose foliation. This alignment shows a direct correspondence between the electrical anisotropy in the subsurface and the geological structure of the area. The cause of electrical anisotropy at the field site was attributed to preferential weathering of weaker mineral bands which were oriented along the strike of schistosity.

Qian and Boerner (1995) studied the EM response of a discretely grounded circuit (DGC) excited by an EM source using an integral equation solution developed by Qian and Boerner (1994). The circuit is representative of man made cultural conductors such as metallic fences, grounded power lines and pipelines. The DGC was modeled by an integral equation which takes into account the mutual interaction between different parts of the circuit. They showed that with an increase in frequency, the effective impedance of the circuit was controlled by the induction of the circuit.

The examples cited here are testimonies to the growth of EM techniques in the newly emerging field of hydrogeophysics. They show the significance of EM methods in characterization of groundwater flow-paths by studying the electrical anisotropies in the EM data.

1.3 Objectives and future chapters

The main goal of this research is to characterize the type of response to be expected from the mutual induction between two targets in a field CSEM experiment. This field of controlled source electromagnetics has not been studied in detail, and hence the effect of mutual coupling between two targets in a CSEM dataset is not well known. Mutual inductance will be modeled using a Texas A&M 3D finite element CSEM code. A number of parameters will be accounted for, such as shape and conductivity of a geological target. In addition to these we also look at the effect of varying transmitter location on the mutual inductance between targets.

Chapter II of this thesis will walk the reader through a brief outline of the theory behind controlled source electromagnetics. A description of field experiments and equipment is also described. The formulation of the CSEM problem, and a description of the 3D CSEM finite element code is provided in chapter II.

Chapter III offers the reader an insight into the concept of mutual inductance and how it applies to cultural targets in a human impacted field site. There is a discussion of the models that have been simulated and the method involved in determining the magnitude of mutual inductance.

In chapter IV, I present the results of the model simulations presented in chapter III. This chapter explores the effect of different parameters on the mutual coupling between two targets, which is achieved by looking at the H_z fields from a variety of models. Parameters that have studied with respect to their influence on mutual coupling include the conductivity, location, shape and orientation of subsurface targets.

Chapter V is a summary of the findings from chapter IV. Here I present my conclusions and discuss the applicability of this research towards groundwater characterization and exploration.

CHAPTER II
THEORY

2.1 Maxwell's equations

The theory of electromagnetic geophysics is based on the following Maxwell's equations which govern the behavior of electromagnetic fields:

$$\nabla \cdot \mathbf{E} = \frac{1}{\varepsilon}\rho \quad ; \tag{2.1}$$

$$\nabla \cdot \mathbf{B} = 0 \quad ; \tag{2.2}$$

$$\nabla \times \mathbf{H} = \mathbf{J} + \varepsilon \frac{\partial \mathbf{E}}{\partial t} + \mathbf{J}_S \quad ; \tag{2.3}$$

$$\nabla \times \mathbf{E} = -\frac{\partial \mathbf{B}}{\partial t} \quad . \tag{2.4}$$

In addition to these, the following two constitutive equations describe the EM properties of conductive and permeable media

$$\mathbf{B} = \mu \mathbf{H} \quad ; \tag{2.5}$$

$$\mathbf{J} = \sigma \mathbf{E} \quad . \tag{2.6}$$

In the above equations,

E = electric field;

B = magnetic flux density;

H = magnetic field;

J = current density in the medium;

Js = current density of source;

μ = magnetic permeability;

ε = dielectric constant;

ρ = volume charge density.

Equation (2.1) is commonly known as the differential form of Gauss's Law which states that the divergence of the electric field **E** over a small closed surface is

directly proportional to the charge density ρ contained within the volume enclosed by the surface.

According to the second equation which can be regarded as the magnetic form of Gauss's law, since magnetic charges (monopoles) have never been observed, the divergence of a magnetic field **B** is set to zero.

The third equation is Ampere's law, as modified by Maxwell. This law states that a current, or time variant electric field vector, will generate a magnetic field vector which curls around the **E** field. The second term on the right side of the equation is the displacement current. This term is safely neglected in EM induction studies since at very low frequencies $\sigma >> \omega\varepsilon$, or equivalently in the time domain

$$|\mathbf{J}| = |\sigma\mathbf{E}| >> \left|\varepsilon \frac{dE}{dt}\right| \quad .$$

Equation (2.4) is Faradays law, which shows that a time variant magnetic field generates an electric field. Eddy currents of density $\mathbf{J} = \sigma\mathbf{E}$ are induced in a material of conductivity σ by the electromotive force associated with the changing magnetic flux. It is important to note that the $\frac{\partial \mathbf{B}}{\partial t}$ term is the essential quantity that generates the eddy current induction process. There is no induction of currents in the magnetostatic case in which $\frac{\partial \mathbf{B}}{\partial t} = 0$.

Equation (2.5) describes how the constituent atomic and molecular magnetic moments in a magnetic material of permeability μ respond to an applied magnetic field, **H.** Equation (2.6) is Ohm's law, which describes how unbound charge carriers such as valence electrons or electrolyte ions migrate in a conductive medium when an electric field is present. In CSEM geophysics, it is Faraday's law and Ampere's law (neglecting displacement current) combined with Ohms law $\mathbf{J} = \sigma\mathbf{E}$ that describes the induction of electric currents in the conductive subsurface.

2.2 Controlled source electromagnetics

In the type of TDEM experiments we consider in this research, an electric current is generated in a transmitter (TX) consisting of a simple loop of wire laid on the ground surface. Upon abrupt switch-off of the current, the primary magnetic field due to the loop current vanishes throughout space and a system of circulating secondary eddy currents is induced within the subsurface in accordance with Faraday's law. These eddy currents diffuse downward and outward, away from the TX loop, similar to the diffusion of a 'smoke ring'. Figure 2.1 shows the decay of the secondary $\mathbf{E}_s$ field. The TX loop in this case is located at the air-ground interface, at the ρ=0 position. The eddy current density in the figure is displayed from 0.1 ms after the time of switch-off of primary current in the TX loop up to 3 ms afterward. The diffusion of the secondary electric field follows an axisymmetric pattern about the z axis, beginning as an image of the TX loop directly beneath the TX which then diffuses away from the TX. The decay of the eddy currents with time generates a "secondary magnetic field". Some of these magnetic field lines pass through a receiver coil and the resulting secondary voltage is recorded. The receiver coil is a loop comprising multiple turns of wire that is laid horizontally on the ground. As magnetic field lines pass through the loop, a secondary voltage proportional to $\frac{\partial \mathbf{B}}{\partial t}$ is generated. Recent Geonics TEM 47 receivers (www.geonics.com) are equipped with 3 component coils, allowing a measurement of horizontal and vertical magnetic fields.

If a highly conductive target is present in the subsurface, the time-varying disturbance in the primary magnetic flux will induce a distribution of eddy currents on the skin of the target. The eddy currents circulate in accordance with Lenz's law. According to Lenz's law, in a time varying primary magnetic field, an electric current is induced such that it generates a secondary magnetic field whose direction is such as to oppose the change in the primary field. In our case, the target responds such as to preserve the total **B** flux through the target that prevailed before the disturbance in the TX loop occurred.

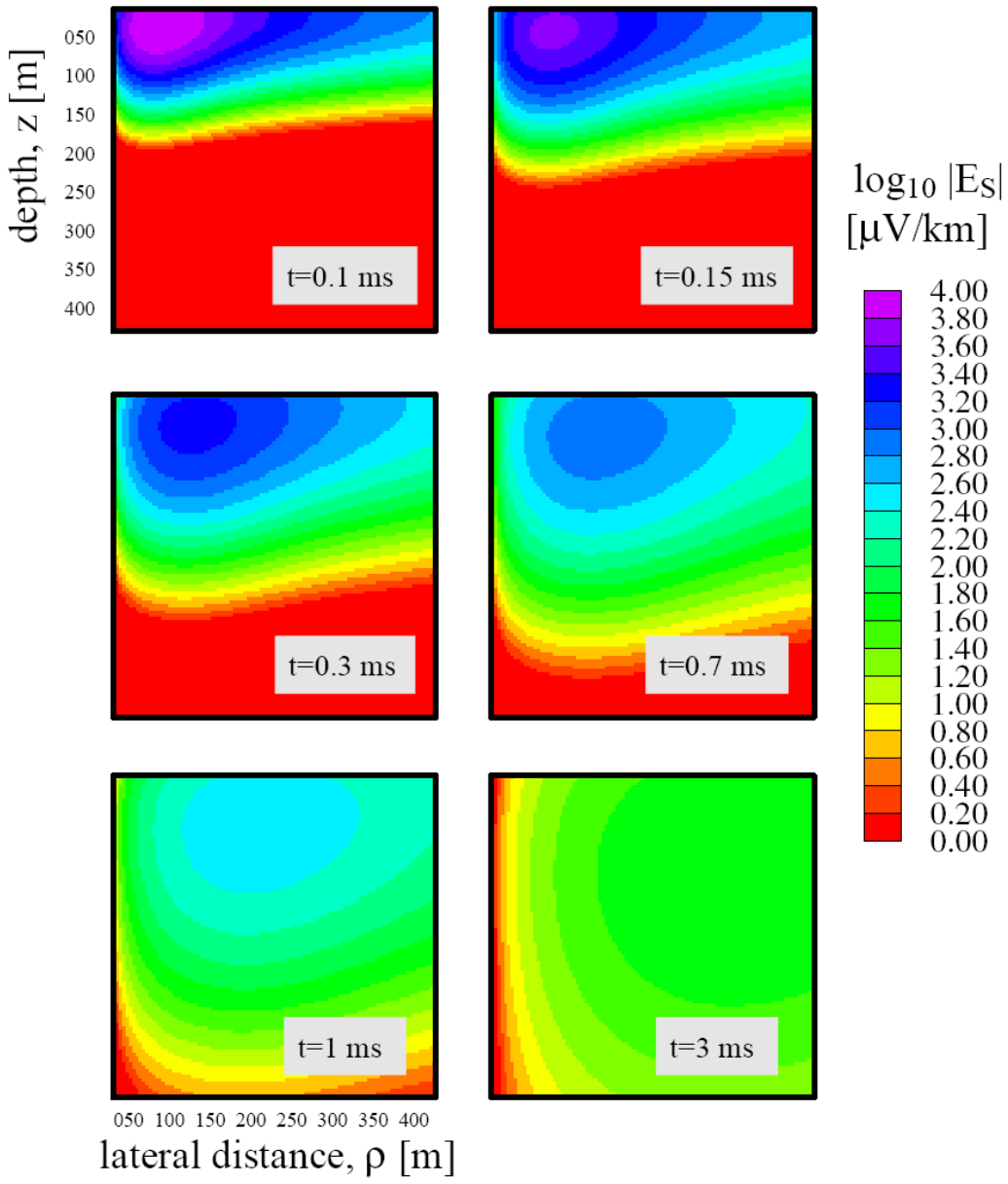

Figure 2.1. Transient smoke ring diffusion into a conducting halfspace, conductivity σ = 0.1 S/m. TX loop is located at ρ= z = 0, on the ground. The figure shows the spreading of the eddy current density $\mathbf{E}_s(t)$ for several times 0.1 < t < 3 ms induced by the abrupt termination at t = 0 of the current in the TX loop (from Everett, 2007).

Once induced, the eddy currents in a conductive target decay with time due to ohmic dissipation and also diffuse toward the center of the target, thus generating a *target magnetic field*.

TDEM involves the reception of the magnetic field from all subsurface currents (host + targets) at different time gates, usually spaced logarithmically to approximately sample the exponential decay. The spacing of the time gates in the Geonics TEM 47 instrument ranges from ~ 7 μs to 0.7 ms after switch-off.

2.3 Apparent conductivity

The voltage or electric field measured at a specific point by a receiver does not give the true conductivity of the geological media at that point or any other single point. Rather, it is a measure of the apparent conductivity. The apparent conductivity is defined as the conductivity of a uniform halfspace whose response matches, as nearly as possible, the observed response. This is because the **E** field measured by the receiver is due to a spatial average of the **E** field within a region of space between the source and the receiver. The extent of the region that contributes to the **E** field in the receiver depends on the frequency of the eddy currents and the actual conductivity distribution of the geological media.

2.4 Skin Depth

The depth to which eddy currents penetrate into a conductive body is given approximately by the skin depth,

$$\delta = \sqrt{\frac{2}{\sigma \mu_0 \omega}} \qquad (2.7)$$

where δ = skin depth , μ_0 = magnetic permeability of free space and ω = angular frequency = $2\pi f$. Equation (2.7) is exact in the case of a plane-wave excitation, which is an approximate representation of the primary field for CSEM at great TX-RX distances such that $\rho >> a$, where ρ is distance from source to receiver and a is radius of transmitter. The skin depth is inversely proportional to the square-root of conductivity.

Thus, currents penetrate deeper into resistive targets as compared to their penetration into conductive targets. Equation (2.7) is a frequency domain expression that assumes harmonic ($\exp +i\omega t$) time dependence of the excitation field. The TDEM method generally uses a step-off excitation, which generates a broadband frequency spectrum. The time-domain equivalent of penetration depth is computed from the *diffusion time,* $\tau = \mu_0 \sigma \rho^2$, which is the time taken for the smoke ring to diffuse from the TX loop to a receiver at distance ρ. The penetration depth of eddy currents at time *t* after switch off is approximately $z \sim \sqrt{\frac{t}{\mu_0 \sigma}}$.

2.5 CSEM surveys

The main components of the equipment involved in a CSEM survey are the transmitter and the receiver. The transmitter loop is a simple insulated wire, while the receiver coil is made up of multiple turns of insulated copper wire. The transmitter box contains a ramp-off signal generator and a current source. The receiver box consists of the receiver coil, amplifier, A/D converter and storage unit.

A transmitter loop of radius ~ 3 m is laid out on the ground to provide the primary magnetic field. Current is made to flow through the current loop as a steady 'on' current. This generates the static primary magnetic field. The steady 'on' in TX current is followed by a sudden linear ramp 'off'. The TX current waveform generated by this switch-off is shown in figure 2.2. The magnetic flux threads through the earth and the emf associated with its abrupt switch off generates eddy currents within the subsurface. The geometry of the eddy current distribution is approximated as an image of the transmitter loop in the subsurface. The eddy current loop moves downward and outward as it diffuses, resembling the shape and motion of a smoke ring. As the currents diffuse, they generate a secondary magnetic field. The secondary magnetic flux is sensed by a receiver coil placed at different locations along a profile line. The RX voltage is recorded at different times. The strength and time evolution of the secondary magnetic field depends on the conductivity of the host and any targets that might be present.

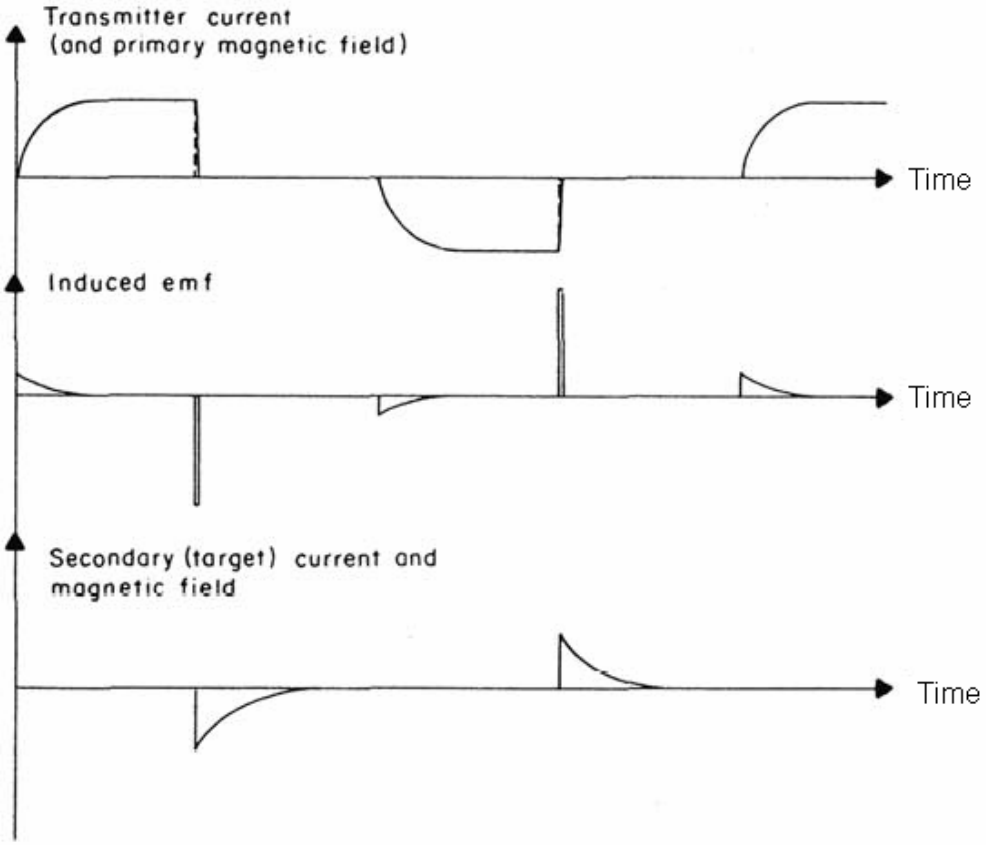

Figure 2.2: The relation of transmitter current (top) with induced emf (middle) and secondary current (bottom) in a halfspace. Observe that induced emf is proportional to the change in TX current with time. (from McNeill, 1980)

.

In a profile type survey, the TX location is held fixed while the TX-RX offset is varied. The spacing between consecutive receiver locations can be uniform or irregular. A RX spacing of ~ 1 m is common in near-surface applications. As the eddy currents generated by the TX diffuse into the subsurface, the RX at higher offsets will sense deeper conductivity structure. A similar concept exists in resistivity sounding, wherein the current electrode spacing is increased to probe to greater depths. The time domain

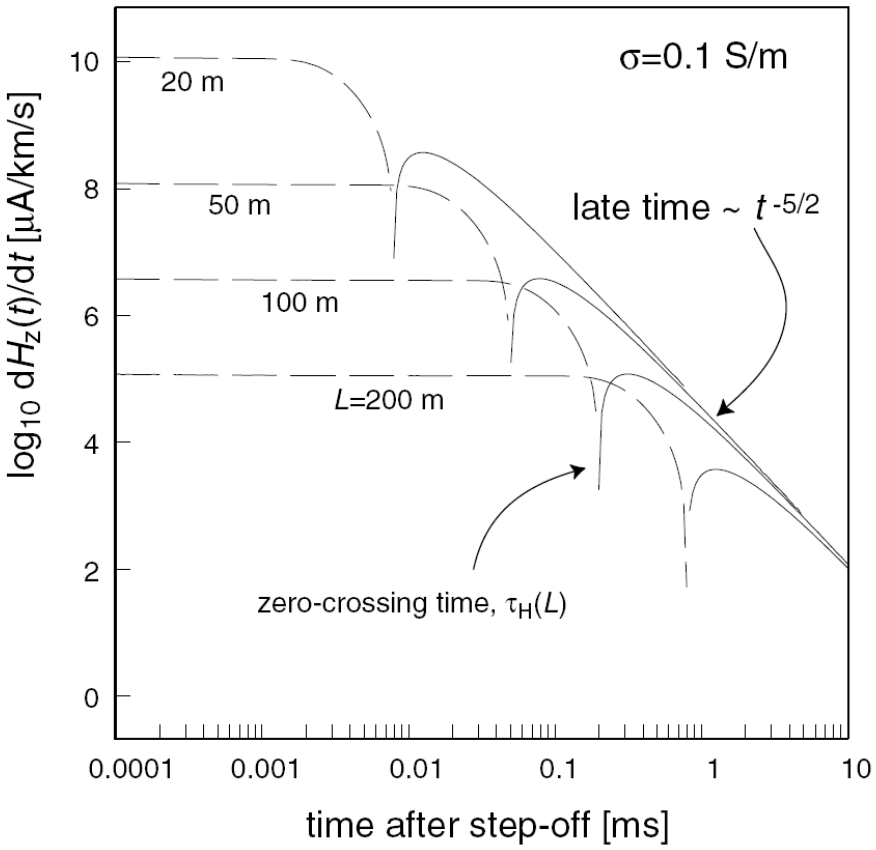

Figure 2.3. Plot of zero crossover times $\tau_H(L)$ for different TX-RX offsets $20 < L <$ 200 m. The zero crossover time is the approximate time at which the eddy currents pass directly under receiver (from Everett, 2007).

equipment uses a broadband signal, such as a sharp linear ramp-off, to achieve deep penetration of current into the earth. Based on the skin depth formula, equation (2.7), the lower frequency signals penetrate deeper into the ground, while the higher frequency components are attenuated close to the surface. An estimate of the apparent conductivity of the ground is obtained by measuring the zero crossing time. The transient receiver voltage approaches zero with increasing time, and then undergoes a change in sign. This

sign change occurs because of a reversal in the direction of the field lines through the RX coil as the secondary eddy currents pass beneath the RX coil. The time at which the voltage passes through zero is called the zero crossover time $\tau_H(L)$ and scales as

$$\tau_H(L) \approx \mu_0 \sigma L^2$$

where L is TX-RX spacing. A plot of RX voltage versus time for different TX-RX separations is shown in figure 2.3.

2.6 Forward modeling

Finite element (FE) and finite difference (FD) techniques have both been used in CSEM modeling endeavors. The FE method operates with an unstructured mesh which can be made to conform to irregular targets (Badea *et al.*, 2001). The FD method on the other hand requires a structured grid. The forward calculations in this thesis of the **E** field is performed using a code written by Dr Mark Everett and further developed by Jack Stalnaker (Stalnaker *et al.*, 2006). A detailed description of the FE formulation is now given.

The diffusive Maxwell's equations for low frequency electric and magnetic fields may be written as

$$\nabla \times \mathbf{E} = i\omega\mu_0 \mathbf{H} \quad ; \qquad (2.8)$$

$$\nabla \times \mathbf{H} = \mathbf{J} = \mathbf{J}_s + \sigma \mathbf{E} \; ; \qquad (2.9)$$

The **E** and **H** fields are conveniently formulated in terms of a magnetic vector potential **A** and an electric scalar potential Ψ as

$$\mathbf{B} = \nabla \times \mathbf{A} \; ; \qquad (2.10)$$

$$\mathbf{E} = i\omega\mathbf{A} - \nabla\Phi \; ; \qquad (2.11)$$

where $\Phi = i\omega \Psi$ is termed the reduced scalar potential. The reduced potential is used to ensure that the FE matrix is symmetric (Biro et al., 1989)

Incorporating equation (2.11) into equation (2.9) gives the curl-curl equation

$$\nabla \times \nabla \times \mathbf{A} = \mu_0 \mathbf{J}_s + \mu_0 \sigma (i\omega\mathbf{A} - \nabla\Phi) \qquad (2.12)$$

Discretization of equation (12) however leads to asymmetric FE matrices. The method of Biro and Preis (1989) overcomes this problem, wherein the term $-\nabla(\nabla.\mathbf{A})$ is incorporated into the above equation to yield

$$\nabla\times\nabla\times\mathbf{A}-\nabla(\nabla.\mathbf{A})-i\omega\mu_0\sigma(\mathbf{A}+\nabla\Psi)=\mu_0\mathbf{A}_s \qquad (2.13)$$

The added term vanishes and equation (2.12) remains unchanged so long as $\nabla.\mathbf{A}=0$ is enforced. This is the Coulomb gauge condition. Equation (2.13) is simplified using the vector identity $\nabla\times\nabla\times\mathbf{A}-\nabla(\nabla.\mathbf{A})=-\nabla^2\mathbf{A}$, which shows that the Coulomb gauged vector potential satisfies the vector Helmholtz equation

$$\nabla^2\mathbf{A}-i\omega\mu_0\sigma(\mathbf{A}+\nabla\Psi)=\mu_0\mathbf{J}_s \qquad (2.14)$$

The discretized form of this equation is numerically stable. Reflecting the fact that no point sources or sinks of electric current in the solution domain, the following auxiliary equation is used,

$$\nabla\cdot[i\omega\mu_0\sigma(\mathbf{A}+\nabla\Psi)]=0 \qquad (2.15)$$

The code used in this research uses a secondary potential formulation by defining a set of known primary EM potentials ($\mathbf{A}_p,\Psi_p$). These primary potentials normally consist of the analytic expression for induction in a homogeneous medium with conductivity σ_p and source current density $\mathbf{J}_p$.

The secondary EM potentials ($\mathbf{A}_{s.}\Psi_s$) are defined as $\mathbf{A}=\mathbf{A}_p+\mathbf{A}_s$ and $\Psi=\Psi_p+\Psi_s$, and satisfy

$$\nabla^2\mathbf{A}_s-i\omega\mu_0\sigma(\mathbf{A}_s+\nabla\Psi_s)=-i\omega\mu_0\Delta\sigma(\mathbf{A}_p+\nabla\Psi_p); \qquad (2.16)$$

$$\nabla\cdot[i\omega\mu_0\sigma(\mathbf{A}_s+\nabla\Psi_s)]=-\nabla.[i\omega\mu_0\sigma(\mathbf{A}_p+\nabla\Psi_p)]\ ; \qquad (2.17)$$

where $\Delta\sigma=\sigma-\sigma_p$ is the difference between the conductivity distribution $\sigma(\mathbf{r})$ whose response is required and the background distribution σ_p (r) whose response is known.

To assemble the finite element system of equations, the 3D domain is discretized into a mesh of non-overlapping polyhedral elements with nodes at the vertices. A mesh generation algorithm then subdivides the 3D domain into tetrahedra.

The secondary EM potentials are expanded into a piecewise linear representation:

$$\mathbf{A_s}(\mathbf{r}) = \sum_{j=1}^{N} A_{sxj}\alpha_j(\mathbf{r})\hat{x} + A_{syj}\alpha_j(\mathbf{r})\hat{y} + A_{szj}\alpha_j(\mathbf{r})\hat{z} \qquad (2.18)$$

$$\Psi_s(\mathbf{r}) = \sum_{j=1}^{N} \psi_{sj}\alpha_j(\mathbf{r}) \qquad (2.19)$$

where $\alpha_j(\mathbf{r})$ is a linear basis nodal function (Everett and Schultz, 1996) associated with node j of the mesh, while $(\mathbf{A}_{sxj}, \mathbf{A}_{syj}, \mathbf{A}_{szj}, \psi_{sj})$ for each of $j = 1\ldots.N$ are coefficients that need to be determined. The number of nodes *N* lie inside the mesh, not including those on the boundary. These equations may be cast into a matrix and then solved.

CHAPTER III
CULTURAL NOISE AND MUTUAL INDUCTANCE

3.1 Cultural noise

In any geophysical experiment, it is rare to have detailed *a priori* information on the subsurface targets since generally they are either the objects of investigation or poorly known sources of cultural noise. It is often useful to carry out a rough reconnaissance survey before a detailed survey is planned in order to shed some light on the nature of the targets. However, parameters such as precise location, conductivity and size of the targets may remain unknown. The problem of 'noise' in the dataset greatly complicates the geological interpretation. Noise may be classified into two types, incoherent noise and signal-generated noise. The first type of noise is attributed to extraneous sources not related to the CSEM experiment. This includes noise from sources such as electric power lines and radio signals. Geomagnetic storms, occurring from violent solar bursts, may also contribute to this type of noise. Other contributions to noise in the dataset include sferics, which is a broadband electromagnetic impulse due to lightning from distant thunderstorms, and the switching of equipment in power generating stations in the vicinity of the CSEM experiment. The signal-generated noise may be defined as noise that is generated by induction in cultural sources due to excitation by the transmitter. For example a buried or outcropping metal body in the presence of a transmitter will contribute an unwanted EM field to the dataset. This inevitably occurs when cultural objects such metal fences, buried pipes or railroad tracks are located in the vicinity of the CSEM experiment. It is important to recognize that cultural noise is temporally coherent with the transmitted signal.

3.2 Mutual inductance

Mutual inductance plays an important role in determining the electromagnetic field in the presence of two or more targets (Stalnaker, 2004). To understand the essential concepts, it is worthwile to examine the following circuit analogy developed by

Purcell (1965). Consider two coils of wire C_1 and C_2 placed arbitrarily in space. Let a constant current I_1 flow through coil C_1 and let the magnetic field generated by that current be $\mathbf{B}_1$ in accordance with Ampere's law.

As figure 3.1 shows, certain amount of this field Φ_{21} will flux through coil C_2.

$$\Phi_{21} = \int_{S2} \mathbf{B} \cdot da_2 \qquad (3.1)$$

where S_2 is any surface whose boundary is the loop C_2 and da_2 is the element of area of surface S_2.

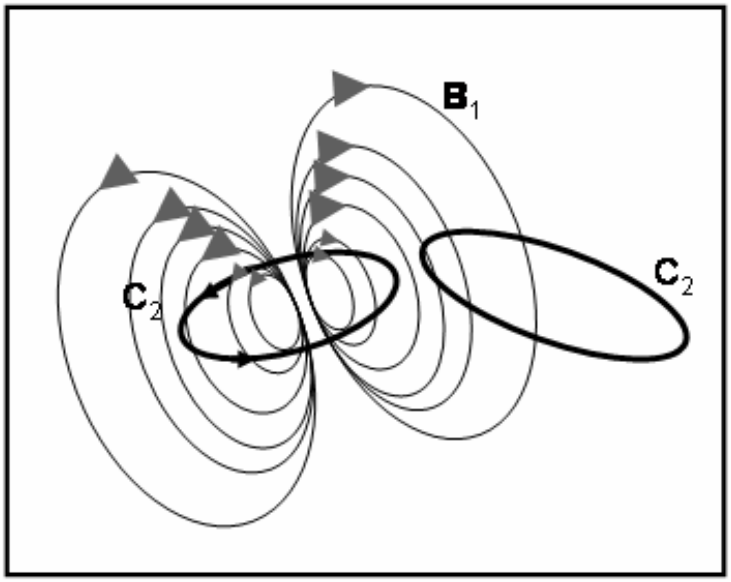

Figure 3.1. Magnetic field $\mathbf{B}_1$ fluxing through loop C_2 due to current flow I_1in loop C_1.

Under these circumstances, the magnetic field $\mathbf{B}_1$ fluxing through coil C_2 is directly proportional to the current I_1 flowing through coil C_1,

$$\frac{\Phi_{21}}{I_1} = cons\tan t\,. \qquad (3.2)$$

Suppose that I_1 changes with time, then the magnetic flux Φ_{21} through loop C_2 will change in proportion as I_1 changes and according to Faraday's law, an electromotive force ε_{21} will be induced in loop C_2 such that

$$\varepsilon_{21} = -M_{21}\frac{dI_1}{dt} \qquad (3.3)$$

where M_{21} is defined in this way as the coefficient of mutual inductance. The quantity M_{21} depends only on the geometry and relative orientation and separation of the loops. In other words, the mutual inductance M_{21} describes the effect of coil C_1 acting as the *source* of the current in coil C_2. The two loops C_1 and C_2 are described as magnetically flux-linked.

The phenomenon of mutual inductance also occurs in field CSEM experiments when more than one target is present. In such cases any one target will act as a source and induce a current in other targets by virtue of their magnetic flux-linkage. Thus, there is a *mutual coupling* between any two targets, wherein one appears as a source of emf to the other.

Consider the case of a TX coil placed on the ground surface with two coils C_1 and C_2 buried at some shallow (~ 1 – 10 m) depth on either side of the TX. These two buried coils represent circuit analogies to the buried volumetric conductors that are encountered in CSEM experiments. Let an alternating current $I^p(t)$ pass through the TX coil. A time varying primary magnetic field $\mathbf{B}^p(t)$ will be generated in accordance with Ampere's law.

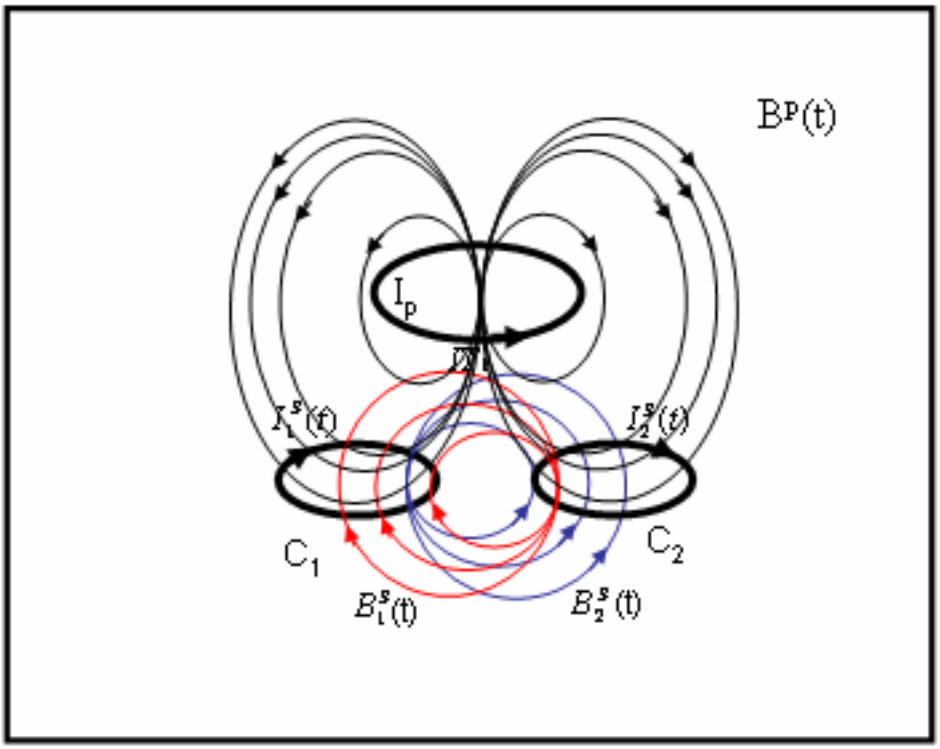

Figure 3.2. Primary and secondary fields associated with a system consisting of a single TX and two buried coils.

Some portion of the primary field will flux through the coils C_1 and C_2. Let $\Phi_1(t)$ be the magnetic field fluxing through C_1 and $\Phi_2(t)$ be the field fluxing through C_2. A general definition of Φ is given by equation (3.1)

Due to the time variation of Φ_1 and Φ_2, secondary emfs will drive currents $I_1^S(t)$ and $I_2^S(t)$ in coils C_1 and C_2, respectively, by Faradays law. These currents generate secondary magnetic fields $\mathbf{B}_1^S$ and $\mathbf{B}_2^S$ respectively. Some part of the secondary field $\mathbf{B}_1^S(t)$ from coil C_1 will flux through coil C_2 and the associated emf generates a

tertiary current I_2^T (t) in coil C_2. Similarly some of the secondary field $\mathbf{B}_2^S$ (t) from coil C_2 will flux through coil C_1 and will induce a tertiary current I_1^T (t) in coil C_1.

Thus the total current in coil C_1 will be given by the sum of secondary and tertiary currents

$$I_1 (t) = I_1^S (t) + I_1^T (t); \quad (3.4)$$

while the total current in C_2 will be given by

$$I_2 (t) = I_2^S (t) + I_2^T (t). \quad (3.5)$$

Equations (3.4) and (3.5) describe how multiple conductors mutually induce tertiary currents in each other. The model described here is a conceptual model using loops, but it is an apt way to describe mutual inductance in a field CSEM survey. The loops in that case represent buried conductors, and calculations of the **E** or **H** field in numerical modeling involve volumetric conductors instead of loops. In this research study, the secondary H_z field is calculated for a series of models using a 3D finite element CSEM code. This code permits the calculation of the secondary H_z field for models involving one or two volumetric conductors.

In order to isolate the effect of mutual coupling between two buried conductors, we write

$$MI = [H_Z^1 + H_Z^2] - H_Z^{(1+2)} \quad (3.6)$$

where MI = mutual coupling

$H_Z^{(1+2)}$ = Magnitude of total magnetic field with two conductors included in the model

H_Z^1 = Magnitude of magnetic field with conductor 1 only

H_Z^2 = Magnitude of magnetic field with conductor 2 only

The output of the 3D finite element CSEM code for any model is the real and imaginary component of the H_Z field along a profile in the *x* direction. To obtain the mutual inductance between two conductors the H_z field for three models must be calculated. The first model includes both conductors which will result in the calculation of the $H_Z^{(1+2)}$ field. The second and third models will calculate H_Z^1 and H_Z^2 which is the

H_z field for a model containing only conductors 1 and 2 respectively. The mutual inductance is then calculated as

$$MI = \sqrt{\mathrm{Re}[H_Z^1 + H_Z^2]^2 + \mathrm{Im}[H_Z^1 + H_Z^2]^2} - \sqrt{\mathrm{Re}[H_Z^{1+2}]^2 + \mathrm{Im}[H_Z^{1+2}]^2} \qquad (3.7)$$

where $\mathrm{Re}[H_Z^{1+2}]$ and $\mathrm{Im}[H_Z^{1+2}]$ are the real and imaginary components of the H_Z field from a model with two conductors, and $\mathrm{Re}[H_Z^1 + H_Z^2]$ and $\mathrm{Im}[H_Z^1 + H_Z^2]$ is the addition of the real component of the secondary field from conductors one and two while $\mathrm{Im}[H_Z^1 + H_Z^2]$ is the addition of the imaginary component of the secondary field from conductors one and two. The expression (3.7) provides a direct estimate of the amount of mutual coupling occurring between two targets because it takes into account the electromagnetic field $H_Z^{(1+2)}$ generated when both targets are present as well as the fields H_Z^1 and H_Z^2 developed when only single targets are present. Essentially, when the secondary response is removed from the dataset, what remains is the tertiary response, or the mutual inductance. MI will also include contributions from the eddy currents induced in the host by the tertiary magnetic fields $\mathbf{B}_1^T(t)$ and $\mathbf{B}_2^T(t)$. There is also a galvanic contribution to MI associated with charge accumulations at the interfaces between the host and the targets. The term MI has the same units as H**,** and can roughly be interpreted as a tertiary magnetic field caused by the tertiary eddy currents.

3.3 Numerical modeling of mutual inductance

To study the effect of mutual coupling, the vertical magnetic field H_z has been simulated for different subsurface conductivity models using the Texas A&M 3D CSEM finite element code. This code calculates the secondary H_z field, which is the field emanating from the conductors in the model. All the model simulations in this research have been performed on the same mesh structure. In order to provide a symmetrical and consistent primary magnetic field for all models, the mesh structure is not changed for any model. A 57 x 57 x 57 node mesh is used, with $x = y = z$ dimensions from -35 m to + 35 m. The spacing between each node is 1.25 m. Care has been taken to ensure that the edges of the slabs modeled match with the location of a node. Each model here has the

same basic structure. There are two halfspaces, an upper halfspace representing air and a lower halfspace representing the earth. The conductivity σ_0 of the upper halfspace is kept at 1 x 10^{-20} S/m, which is a very low conductivity, representing an air layer. There are two slabs in the lower halfspace, which will mutually induce tertiary currents in each other. The slabs have been modeled to represent either a geological heterogeneity such as a fracture or a cultural conductor such as a metal plate or slab, depending on the conductivity. The mutual coupling (MI) has been calculated using equation (3.7). In order to accomplish this, the H_z field has been calculated for the case of both slabs in the model and the cases with the model containing only individual slabs. This will give the $H_Z^{(1+2)}$, H_Z^1 and H_Z^2 fields respectively, which are then used in equation (3.7) to calculate the MI.

The code uses a quasi minimum residual (QMR) iterative solver to calculate the H_z field for each model. The maximum number of iterations chosen for the models is 650 and a cut-off residual of 10^{-25} has been selected.

In this research, different parameters such as the slab conductivity, the offset between conductors and the location of TX relative to conductors have been studied and the results are presented in the next chapter.

Several suites of models will now be described. Each suite is designed to provide a unique insight into the mutual inductance process. A brief outline of each model suite is presented below in table 3.1. These models are then discussed in more detail.

Table 3.1 : Classification of models used in calculation of mutual inductance

Model suite	Model series	σ_L (S/m)	σ_R (S/m)	Varying parameter	L(m)	TX location	Frequencies
A	1	0.01	0.01	$\sigma_L = \sigma_R$ = variable	10	middle	1, 10, 20, 100, 500 KHz
A	2	0.04	0.04	$\sigma_L = \sigma_R$ = variable	10	middle	1, 10, 20, 100, 500 KHz
A	3	0.05	0.05	$\sigma_L = \sigma_R$ = variable	10	middle	1, 10, 20, 100, 500 KHz
A	4	0.1	0.1	$\sigma_L = \sigma_R$ = variable	10	middle	1, 10, 20, 100, 500 KHz
A	5	0.2	0.2	$\sigma_L = \sigma_R$ = variable	10	middle	1, 10, 20, 100, 500 KHz
A	6	1	1	$\sigma_L = \sigma_R$ = variable	10	middle	1, 10, 20, 100, 500 KHz
B	1	0.001	0.1	σ_L	10	middle	0.5, 1 , 2 KHz
B	2	0.002	0.1	σ_L	10	middle	0.5, 1 , 2 KHz
B	3	0.005	0.1	σ_L	10	middle	0.5, 1 , 2 KHz
B	4	0.01	0.1	σ_L	10	middle	0.5, 1 , 2 KHz
B	5	0.02	0.1	σ_L	10	middle	0.5, 1 , 2 KHz
B	6	0.05	0.1	σ_L	10	middle	0.5, 1 , 2 KHz
B	7	0.1	0.1	σ_L	10	middle	0.5, 1 , 2 KHz
C	1	0.1	0.1	TX position	10	far field	0.5, 1 , 2 KHz
C	2	0.1	0.1	TX position	10	directly above LHS	0.5, 1 , 2 KHz
C	3	0.1	0.1	TX position	10	middle	0.5, 1 , 2 KHz
D	1	0.05	0.1	TX position	10	far field on LHS	0.5, 1 , 2 KHz
D	2	0.05	0.1	TX position	10	directly above LHS	0.5, 1 , 2 KHz
D	3	0.05	0.1	TX position	10	middle	0.5, 1 , 2 KHz
D	4	0.05	0.1	TX position	10	directly above RHS	0.5, 1 , 2 KHz
D	5	0.05	0.1	TX position	10	far field on RHS	0.5, 1 , 2 KHz
E	1	0.01	0.1	TX position	10	far field on LHS	0.5, 1 , 2 KHz
E	2	0.01	0.1	TX position	10	directly above LHS	0.5, 1 , 2 KHz
E	3	0.01	0.1	TX position	10	middle	0.5, 1 , 2 KHz
E	4	0.01	0.1	TX position	10	directly above RHS	0.5, 1 , 2 KHz
E	5	0.01	0.1	TX position	10	far field on RHS	0.5, 1 , 2 KHz
F	1	0.1	0.1	left-hand slab shape	10	middle	0.5, 1 , 2 KHz
F	2	0.1	0.1	left-hand slab shape	10	middle	0.5, 1 , 2 KHz
F	3	0.1	0.1	left-hand slab shape	10	middle	0.5, 1 , 2 KHz
G	1	0.05	0.1	left-hand slab shape	10	middle	0.5, 1 , 2 KHz

Table 3.1: Continued.

Model suite	Model series	σ_L (S/m)	σ_R (S/m)	Varying parameter	L(m)	TX location	Frequencies
G	2	0.05	0.1	left-hand slab shape	10	middle	0.5, 1 , 2 KHz
G	3	0.05	0.1	left-hand slab shape	10	middle	0.5, 1 , 2 KHz
H	1	0.01	0.1	left-hand slab shape	10	middle	0.5, 1 , 2 KHz
H	2	0.01	0.1	left-hand slab shape	10	middle	0.5, 1 , 2 KHz
H	3	0.01	0.1	left-hand slab shape	10	middle	0.5, 1 , 2 KHz

Model suite A

This model series suite attempts to compare the magnitude of the mutual inductance for conducting slabs of varying conductivity. For each simulation, the model is composed of a halfspace with conductivity 0.02 S/m. There are two slabs in the model, with identical conductivity. The dimensions of both slabs are 1.25 m x 10 m x 5 m in the *x, y* and *z* directions, respectively, and they are separated by a distance of 10 m in the *x*-direction. Both slabs are buried so that the top of each slab is 5 m below the halfspace. The primary field is supplied by a TX loop of radius 3 m located between the two slabs at the top of the lower halfspace, which provides a 1 amp current. An illustration of this model suite is provided in figure 3.3.

The conductivity of each slab varies from 0.01 S/m to 1 S/m. Each model has been simulated for frequencies of 1, 10, 20, 100, and 500 KHz. This simulation will give us an idea of the robustness of the code. Numerical simulations are sometimes limited by certain parameters such as frequency and the broad range of frequencies used here will enable us to determine the stability limits of the code. The finite element solutions can break down at high frequencies or at high target/host conductivities

The main aims for using this model suite are

1. to study the effects of conductivity on mutual inductance between two targets with the same conductivity;
2. to examine the numerical stability of the code;

3. to better understand the role of frequency in determining the mutual inductance between two conductors.

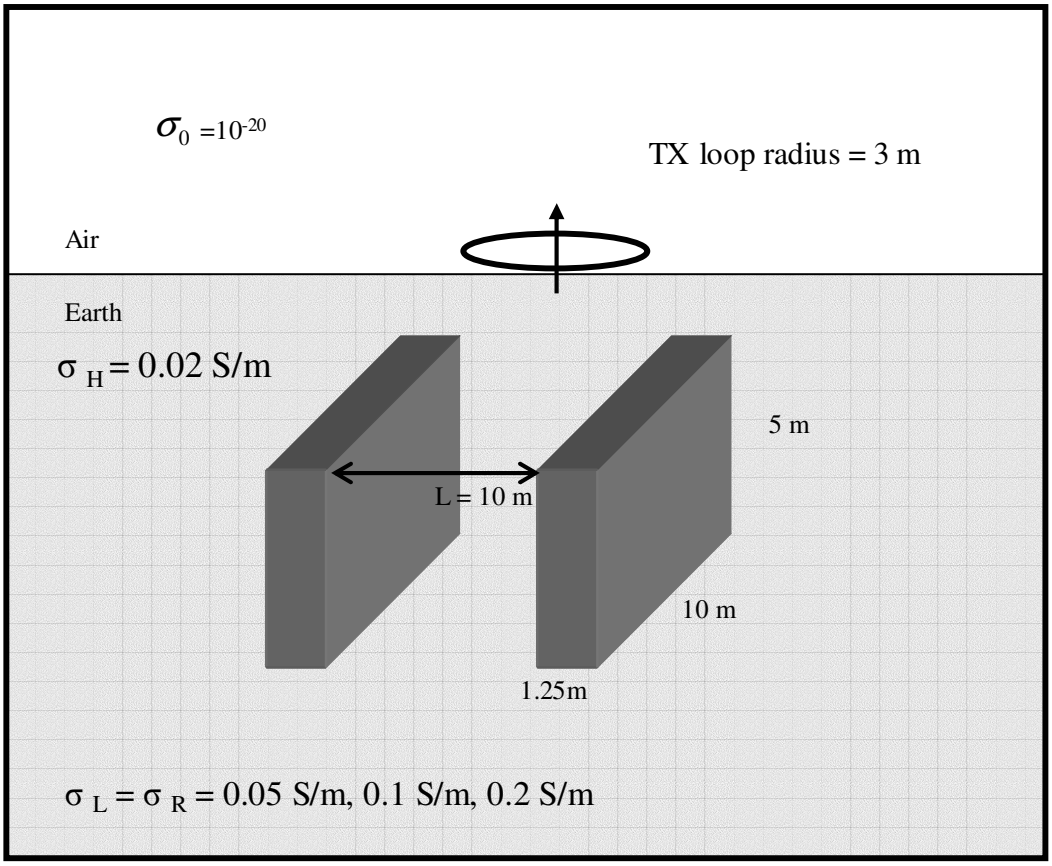

Fig 3.3. Model suite A.

Model suite B

In this suite of models, the H_z field is simulated for a halfspace with two similar slabs, as shown in figure 3.4. However for each simulation, the conductivity of the left-hand slab is varied, while the other is kept constant at 0.1 S/m. The halfspace again has a conductivity of 0.02 S/m. The two slabs modeled here have the same dimensions as suite A. The separation distance between the two slabs is 10 m in the *x* direction. The depth to the top of each slab is 5 m. A TX loop of radius 3 m is used in each case to provide a primary TX current of 1 amp. It is situated in between the 2 slabs.

The aim of this model suite is to better understand how the mutual inductance changes when a known cultural conductor is present in the vicinity of a geological heterogeneity such as a fracture. To accomplish this goal, the right hand side slab has a fixed large value of conductivity (0.1 S/m) representative of a metal plate while the conductivity of the left hand side is varied from 0.001 S/m to 0.1 S/m. This range of conductivities has been selected to simulate different geological features. The left-hand slab with lower conductivities (0.001 S/m to 0.005 S/m) represents a resistive heterogeneity. This is often the case with air-filled fractures. The wider the fracture, the lower the effective conductivity. Higher conductivities in the left-hand slab (0.01 S/m to 0.05 S/m) represent geological features such as water filled fractures or clay filled fractures, both of which have the effect of increasing the effective conductivity of the heterogeneity. The highest conductivity used for the left-hand slab is 0.1 S/m, which matches the conductivity of the right-hand slab representing the buried cultural feature.

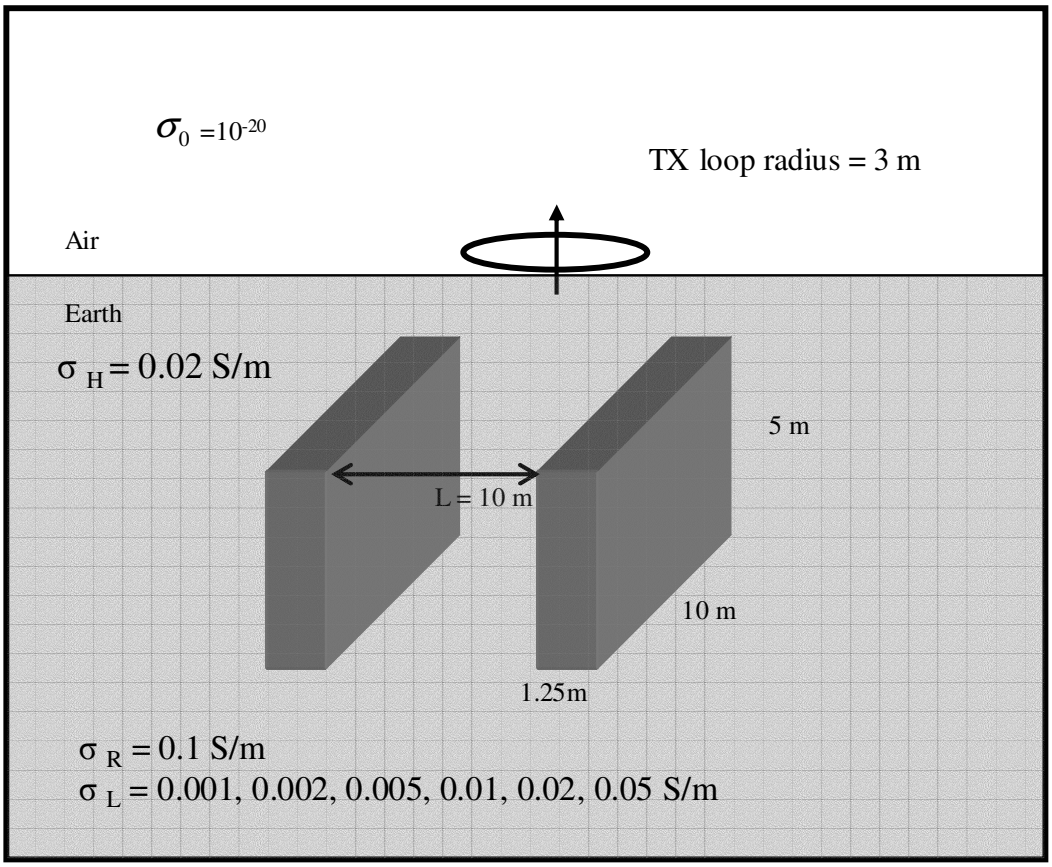

Figure 3.4. Model suite B, varying conductivity of left-hand slab.

Model suite C

Three different cases are studied here. The model used is a halfspace containing two identical slabs. The location of the TX varies in the *x* direction (along a profile line) with respect to the conductors. As shown in figure 3.5, the TX could either be

- at a large distance away from both conductors
- directly above one of the conductors
- in between the 2 conductors

The model uses two slabs of identical conductivity in all cases so that the effect of varying the TX position may be isolated. The conductivity used for the slabs is $\sigma_L = \sigma_R =$ 0.1 S/m. Dimensions of the slab are the same as model suite A. The two slabs are separated by a distance of 10m in the x-direction.

The case in which the TX is located away from both conductors is one that is most probable in the field. When the location of closely spaced targets is unknown, a profile type survey will most likely include the case of the TX located at a large distance away from the targets. It is expected that the conductor closer to the TX will act as a relatively powerful secondary source of the **E** field and will induce a relatively strong tertiary current in the other conductor.

In the second case, the TX is located directly above one of the conductors. The model used here is identical to the above model, with two slabs of conductivity 0.1 S/m, spaced 10 m apart.

A third scenario is characterized by the TX located between the two conductors. This situation has been modeled with the TX located exactly between the 2 slabs. Again, the model is made up of two slabs with conductivity 0.1 S/m, located 10 m apart.

Due to the symmetry of the models, the case of a TX located directly above the right-hand slab or at large distances away from the slabs on the right and side will be similar to the cases already discussed. The results will be a ‘mirror image’ of the graphs from the models already discussed in this suite.

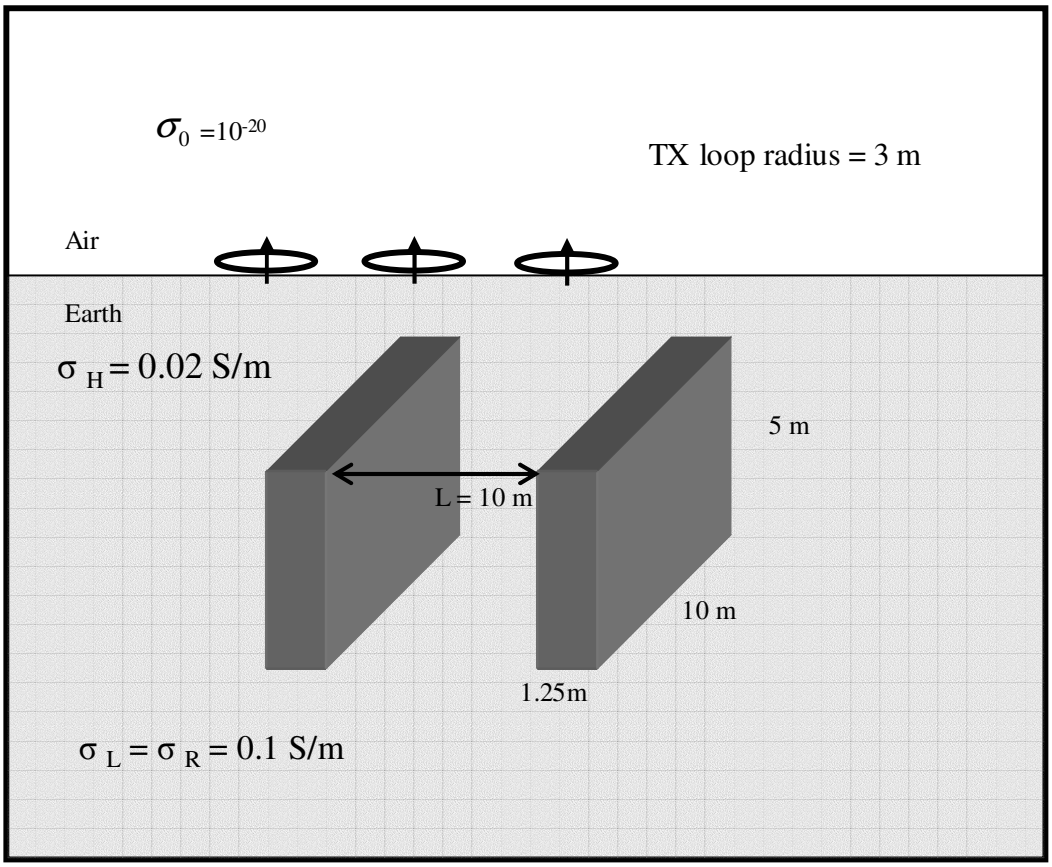

Figure 3.5. Model suite C, showing different TX positions along the *x*-direction.

Model suite D

This model suite is similar to the suite D because again, the goal is to study the effect of different TX locations along a profile type survey across the slabs, illustrated in figure 3.6. The difference between the two models is that in this case, the slabs in each model have different conductivity. The dimensions of the slabs are identical to those of model suite C, and are located 10 m apart. The depth to the top of each slab is 5 m. the conductivity of the left-hand slab is 0.05 S/m, which is representative of a clay or water filled fracture, while the conductivity of the right-hand slab is 0.1 S/m, representing a metal target. As in the previous model suite a TX loop of radius 3 m carrying a current of 1 amp is used to supply the primary magnetic field.

In order to model the tertiary field from a profile type survey for this suite, the following TX locations should be accounted for:

- at a large distance away from both conductors on the left-hand, closer to the fracture;
- directly above the fracture;
- in between the fracture and metal plate;
- directly above the metal plate;
- at a large distance away from both conductors on the right-hand side, closer to the metal plate.

It is particularly interesting to see how the results from this model suite differ from the previous one because the conductivity of geological media differs from that of a cultural body. It is also important to note that the left-hand slab conductivity for this suite is greater than the host conductivity. There is the possibility that in a field experiment the geological media may include features such as an air filled fracture which will have a lower conductivity than the host. This situation is modeled in suite E.

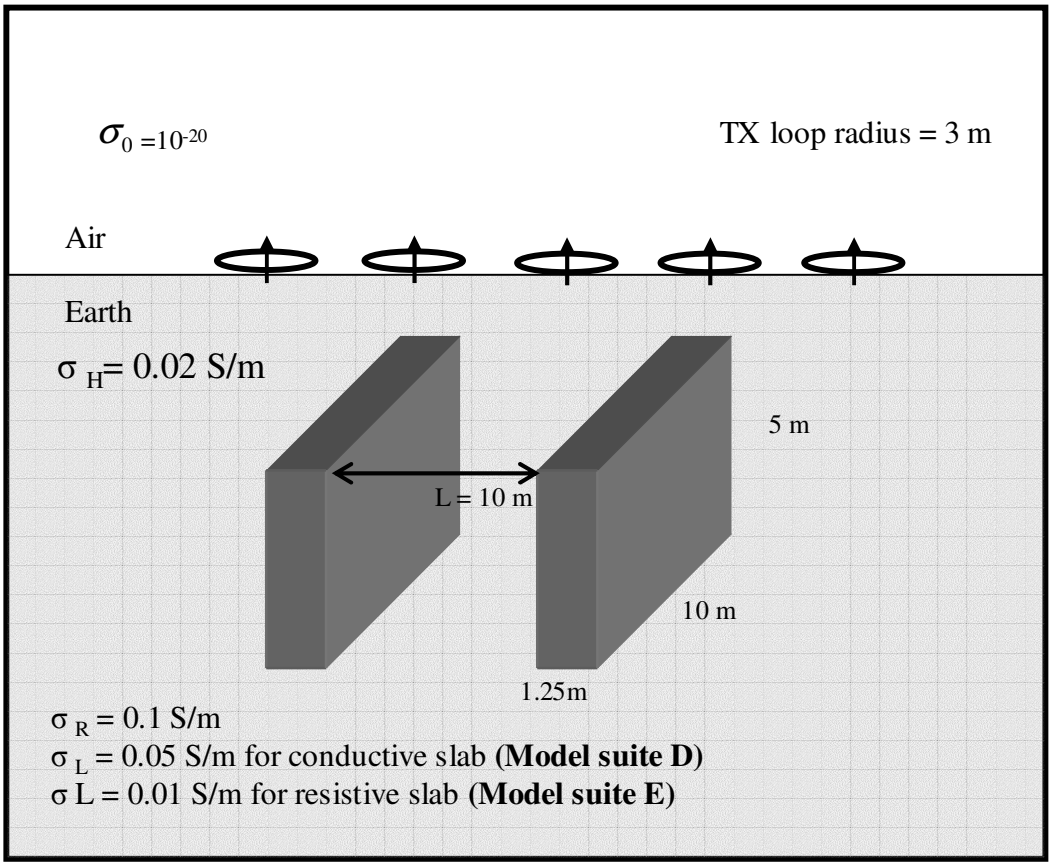

Figure 3.6. Model suites D and E , showing different TX positions along the *x*-direction for slabs of varying conductivity, with $\sigma_L > \sigma_H$ for model suite D and $\sigma_L < \sigma_H$ for model suite E.

Model suite E

This model suite is identical to the previous model suite, except that in this case the left-hand slab conductivity σ_L has been decreased from 0.05 to 0.01 S/m. This is done so that the geological feature represented by the left-hand slab has a conductivity lesser than the host conductivity σ_H. This will make it a resistive body, which includes features such as an air filled fracture. Again, to properly simulate the tertiary field from this model suite, the following TX locations are modeled :

- at a large distance away from both conductors on the left-hand side, closer to the fracture;
- directly above the fracture;
- in between the fracture and metal plate;
- directly above the metal plate;
- at a large distance away from both conductors on the right-hand side, closer to the metal plate.

The illustration for this model suite is presented in figure 3.6, along with that of model suite D.

Model suite F

This model series suite examines how the mutual inductance changes with the shape of a conductor. The basic two slab model from the previous model suites is preserved. However, the shape and/or orientation of the left-hand slab is altered. Three different scenarios are modeled in this suite, a model with horizontal left-hand slab, a long vertical left-hand slab, and a cube of length 2.5 m. The idea behind modeling the different shapes stems from the fact that geological heterogeneities in a field site may have a variety of shapes and orientation. In addition to this, if two or more cultural targets are present in the subsurface, it is probable that the shapes and orientation of the targets will differ. For example, consider the human impacted Honey creek field site in Boerne, Texas, that motivated this research. In this case a multitude of cultural sources were present within a very limited area. These included metal sheets, compact metal objects such as water pumps, and one dimensional objects such as water sprinklers rooted in the ground. This model suite considers the mutual coupling between two cultural targets because both slabs in this suite have been a conductivity of 0.1 S/m.

The first model has a left-hand horizontal slab and a right-hand vertical slab, as shown in figure 3.7 with conductivities 0.1 S/m spaced 10 m apart. Volumetrically, the slabs are equal; the only difference between the two slabs being that the left-hand slab is placed on its side. The depth to the top of both slabs is 5 m. This model series is representative of a host of situations in a human impacted field site. For example the metal sheeting associated with building foundations may be numerically simulated as a buried horizontal slab.

The second model, or model series 2, has 2 vertical slabs, but the left-hand slab is longer than the right-hand slab. The length of the left-hand slab in the z direction is 10m, while the right-hand slab has a height of 5 m. The separation distance between the 2 slabs is 10 m. This model is illustrated in figure 3.8.

The third model, shown in figure 3.9 is composed of the right-hand slab from the previous model, and a left-hand cube of conductivity 0.1 S/m spaced 10 m apart. The length of the cube is 2.5 m, and the conductivity of both slabs is 0.1 S/m.

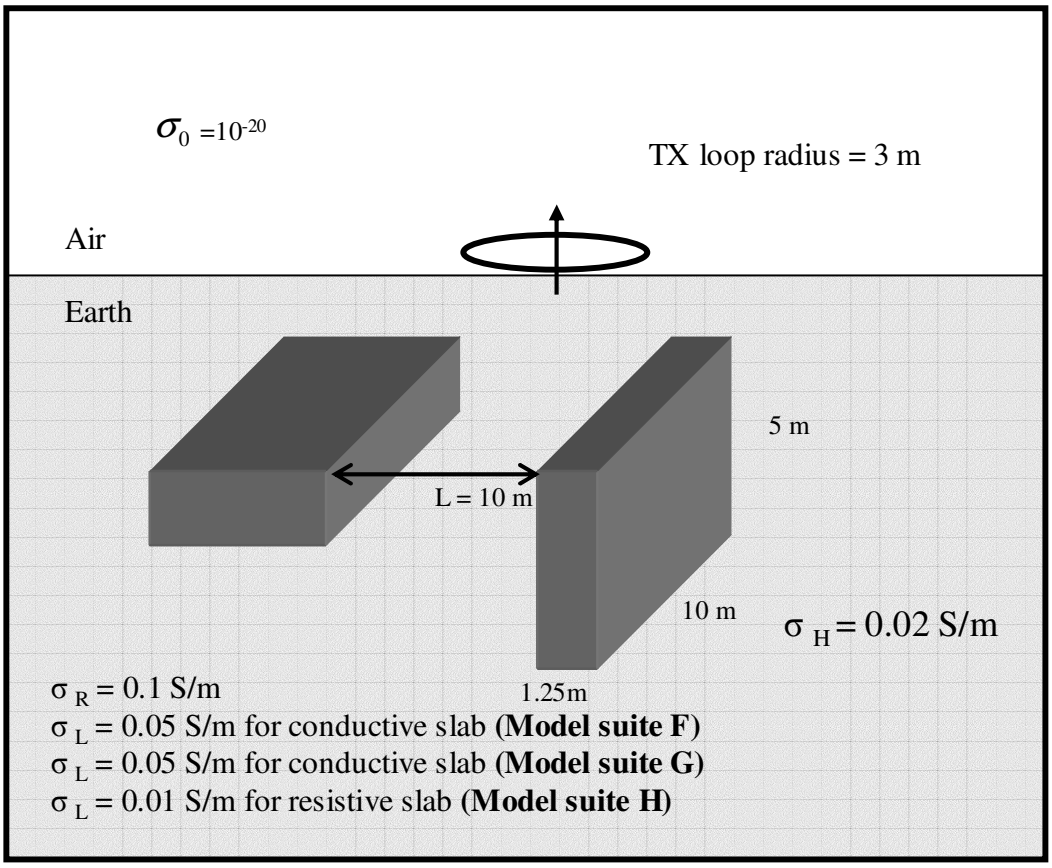

Figure 3.7. Model suites F, G and H, series 1 with left-hand slab horizontal.

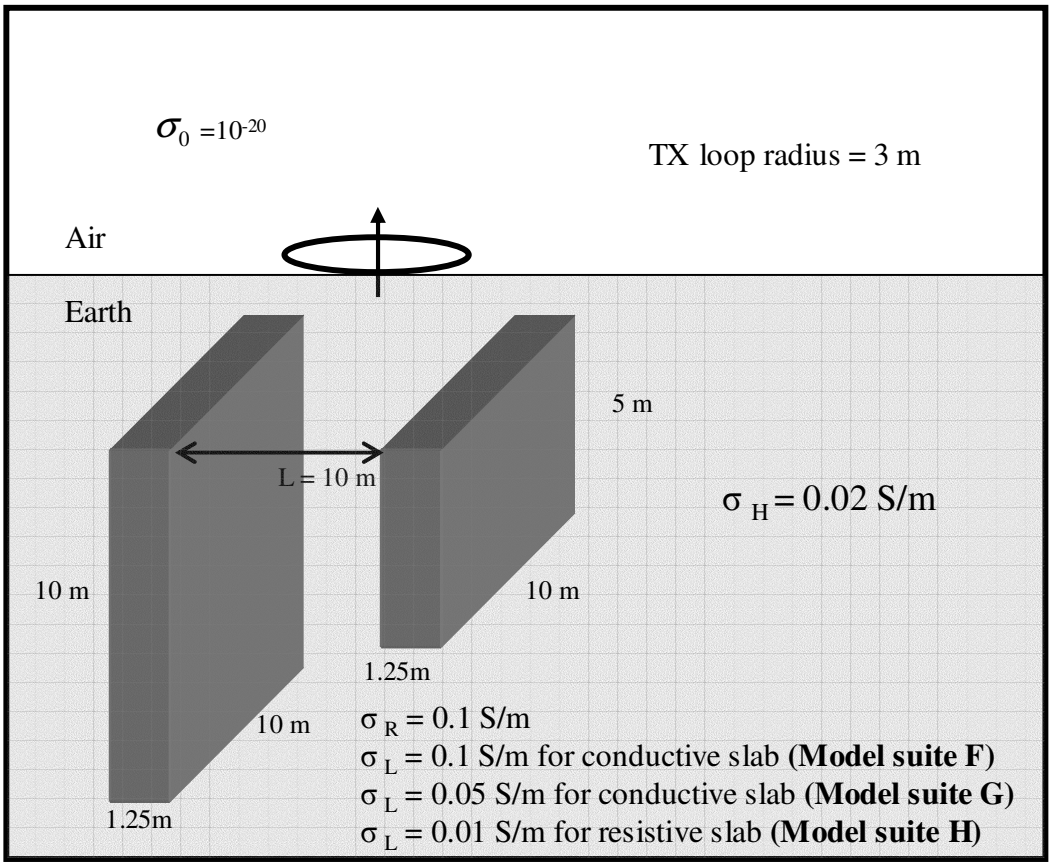

Fig 3.8. Model suites F, G, and H, series 2 with left-hand slab longer than right-hand slab.

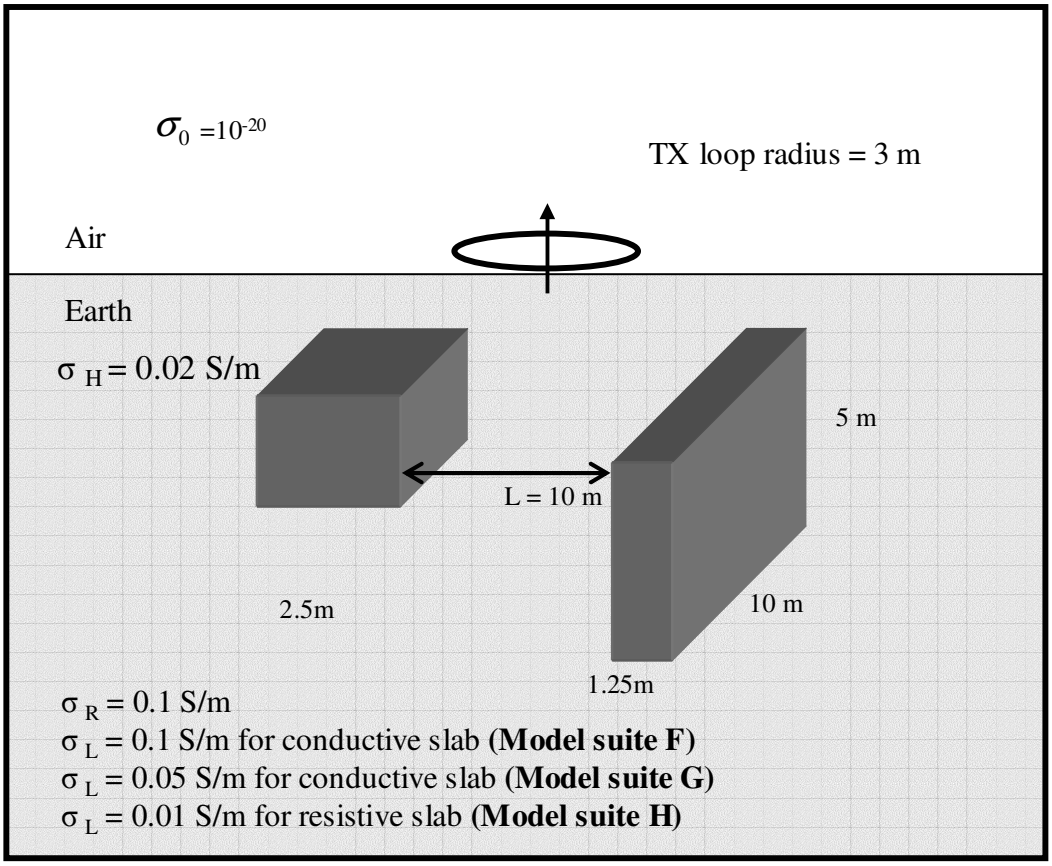

Figure 3.9. Model suites F, G and H, series 3 with left-hand cube.

Model suite G

The models in this suite are also two slab models, designed to look at the mutual inductance between conductors of different shape. The three models presented here have the same dimensions as those in model suite F, however the conductivity of the left-hand slab is 0.05 S/m. It is thus conductive with respect to the host which has a conductivity of 0.02 S/m. The right-hand slab in this model suite is the same as that used for all the previous models. The source for the primary field is a TX loop of radius 3 m located at $x = y = 0$, carrying a 1 A current. The illustrations for these models are presented in figures 3.7, 3.8 and 3.9.

Figure 3.7 shows the first model for this series, where the left-hand slab is horizontal and depth to the top of the slab is 5 m. The left-hand slab is volumetrically identical to the right-hand slab.

The second model is presented in figure 3.8. As in the previous model suite, the left-hand slab for this model is vertical and has a height of 10 m. Both slabs are buried at a depth of 5 m.

In the third model of this suite, the left-hand slab is represented as a cube of length 10 m, which is buried at a depth of 5 m. This model is shown in figure 3.9.

Model suite H

The models present in this suite are similar to those in the previous two model suites, except that the conductivity of the left-hand slab is changed to 0.01 S/m. The host conductivity is 0.02 S/m, and is greater than the conductivity of the left-hand slab. The right hand slab is identical to the right-hand slabs used in previous models, and is representative of a cultural conductor with a conductivity of 0.1 S/m. As in the previous model, the shape of the left-hand slab is changed. This model suite will be used to look at the mutual induction between a resistive body and a cultural target. The three models from this suite are presented below.

Figure 3.7 shows the first model for this series, where the left-hand slab is horizontal and depth to the top of the slab is 5 m. The left-hand slab is volumetrically identical to the right-hand slab.

The second model is presented in figure 3.8. As in the previous model suite, the left-hand slab for this model is vertical and has a height of 10 m. Again, both slabs are buried at a depth of 5 m.

The last model of this suite uses a cube of length 2.5 m as the left-hand slab. The depth to the top of both targets is 5 m. The resistive cube is representative of a compact geological feature such as a sinkhole. The model is illustrated in figure 3.9.

As discussed previously, for each of the models presented in this chapter, a total of three H_z calculations have been performed to obtain the $H_Z^{(1+2)}$, H_Z^1 and H_Z^2 fields and the mutual inductance is then calculated using equation (3.7). The results of these model simulations is presented in chapter IV.

CHAPTER IV
RESULTS AND DISCUSSION

4.1. EM response from single slab

In this chapter, I present the results for calculation of mutual inductance from the models presented in chapter III. The MI for each of the model suites is presented separately, and the distance vs MI graphs are plotted for different frequencies. Before analyzing the electromagnetic interaction between two conductors, it is interesting to first look at the H_z field from a single conductor. Analyzing the simpler scenario of one conductor will provide insights needed to understand the more complicated scenario of two conductors. Figure 4.1 (a) and (b) represent the real and imaginary parts of the secondary H_z field from a single conductor buried at a depth of 5m and located 5 m away on the left-hand side of a source at location $x=y=z=0$. The dimensions of the slab are 1.25 m x 10 m x 5 m. Thus, the slab is vertical and elongated in the $\pm y$ directions. The conductivity of the slab has been selected so that in one case it represents a conductive target with σ = 0.1 S/m while in the other, it is representative of a resistive target with σ = 0.001 S/m. The host conductivity is σ_{host} = 0.02 S/m. The basis for determining whether a slab is conductive or resistive depends on the host conductivity. For the conductive slab, $\sigma_{slab} > \sigma_{host}$ while for the resistive slab $\sigma_{slab} < \sigma_{host.}$ Figure 4.1 show that for both, the real and imaginary components, the H_z field is stronger over the conductive target. This is to be expected because the conductive target is able to sustain a stronger system of secondary currents than the resistive target. Interestingly, for both, the real and imaginary components, the shape of the resistive curve is opposite to that of the conductive curve. The conductive curve has a positive peak slightly to the right, above the slab, while the resistive curve shows a negative peak at the same location. The opposite sign of the fields indicates that the induced currents flow in opposite directions within conductive and resistive targets. The shape of the real and imaginary components of the two fields, which is consistent with the shape of the field from a vertical magnetic dipole. Thus, we can conclude that the secondary currents induced in the slabs are

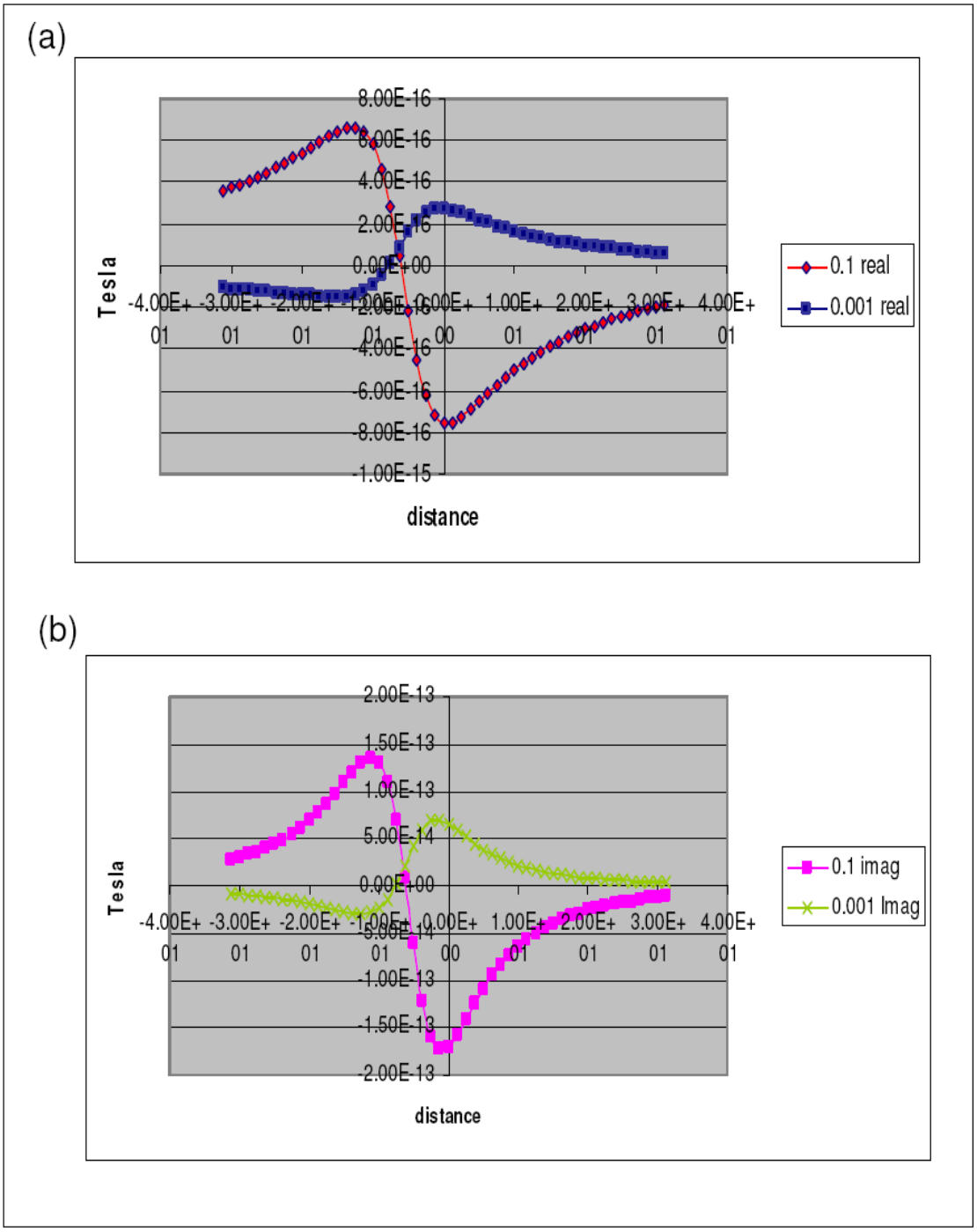

Figure 4.1. Real (a) and imaginary (b) parts of H_Z field for resistive and conductive targets located to the left of the source.

predominantly in the *y-z* plane, which is the plane with maximum surface area. To understand why the fields have opposite signs, I first look at the induction of secondary currents in the slab by the primary magnetic field. Since both slabs are at the same location, I expect an identical flux of primary magnetic field through both slabs.

Figure 4.2 shows the induction of secondary currents in a resistive and conductive slab. The currents induced in the slabs circulate in opposite directions. To better understand this, consider the conductivity of the slabs with respect to the host conductivity. It is seen that with respect to the host conductivity, the resistive slab has a negative conductivity, while the conductive slab has a positive conductivity. Let us consider the effective conductivity of a slab to be the difference between the true conductivity of the slab and the host conductivity.

For the case of the conductive slab, this effective conductivity is calculated as $\sigma_{EC} = \sigma_{slab} - \sigma_{host} = 0.1 - 0.02 = 0.08$ S/m. For the resistive slab, this effective conductivity is $\sigma_{EC} = \sigma_{slab} - \sigma_{host} = 0.001 - 0.02 = -0.019 S/m$. Notice that the effective conductivity of the conductive and negative slabs have opposite signs.

Now consider what happens when the secondary currents are induced by the primary $\mathbf{B}$ field. According to Faraday's law, $\nabla \times \mathbf{E} = -\frac{\partial \mathbf{B}}{\partial t}$. However, since $\mathbf{J} = \sigma \mathbf{E}$, we can write Faraday's law as $\nabla \times \frac{\mathbf{J}}{\sigma} = -\frac{\partial \mathbf{B}}{\partial t}$.

Thus, if σ is negative, the induced secondary currents will flow in on opposite direction to the case when σ is positive.

It is important to note that a 'negative conductivity' does not actually exist. Any conductivity value is always positive. However, a negative effective conductivity can certainly exist. The concept of negative conductivity is employed here to better explain the sign difference in the H_z fields for the resistive and conductive slabs, and to stress on the significance that the host conductivity plays on these H_z fields.

The forthcoming figures represent the mutual inductance for the models described in chapter III.

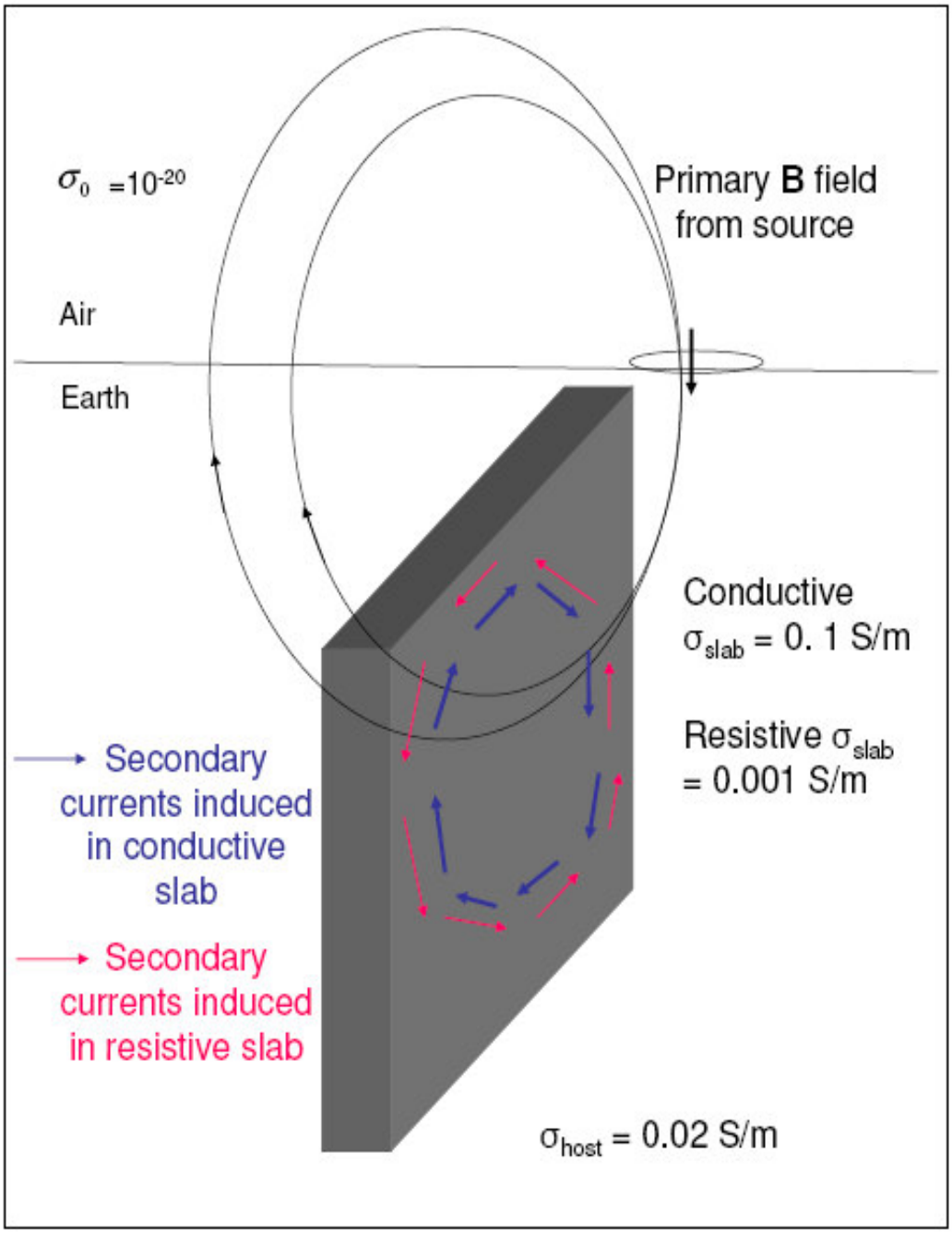

Figure 4.2 : Induction of secondary currents in a conductive vs resistive slab.

4.2. Model suite A

Figures 4.3 and 4.4 show the mutual inductance vs distance for two identical slabs placed 10 m apart, at three different frequencies. Both slabs have same conductivity. All models here have slabs with a positive effective conductivity, wherein $\sigma_{slab} > \sigma_{host}$.

Figure 4.3 shows the MI plot for a frequency of 1 KHz. An inspection of the plot indicates that MI is greater for slabs with higher conductivities as opposed to slabs with lower conductivities. The MI for the model with slab conductivity 0.2 S/m is 2 x 10^{-14} *T* while for the slabs with lower conductivity 0.05 S/m it is 0.1 x 10^{-14} Tesla. For all three conductivities, it is seen that there is a peak at the $x = 0$ position. This is where maximum mutual inductance occurs, and this may be expected because of the symmetry of the slabs on either side of the TX located at the zero position. There are two smaller peaks at positions just beyond the slabs. These may be better explained in terms of a quasi dipole field where the two slabs act as quasi dipoles due to induction by the primary field. The dipoles in this case are oriented vertically in the *y*-*z* plane. This theory also explains why the MI tends to approach zero at far offsets, because further away from a dipole, the field will decrease in magnitude until it vanishes at some offset. An illustration of the tertiary currents developed in the slabs is presented in Figure 4.3. To better understand how these fields are generated, consider first the primary field emanated from the TX. As seen in Figure 4.2, the primary current in the TX is in a clockwise direction for a conductive slab, causing the primary magnetic field $\mathbf{B}^{P}(t)$ to flux through the loop in a downward direction. As this field fluxes through the left-hand slab, the field lines are oriented in the $+z$ and $-x$ direction. They are tilted downward and flux through the slab from right to left. This induces a set of secondary currents $I_1^S(t)$ in the left-hand slab that circulate in a clockwise direction, and is tilted to the right. The secondary magnetic field generated by these currents will flux through the right-hand slab from left to right, and will be tilted upwards. This magnetic flux through the right-hand slab will induce a set of tertiary currents in the slab, which will circulate in a counter clockwise direction and is tilted to the right. The tertiary magnetic field induced

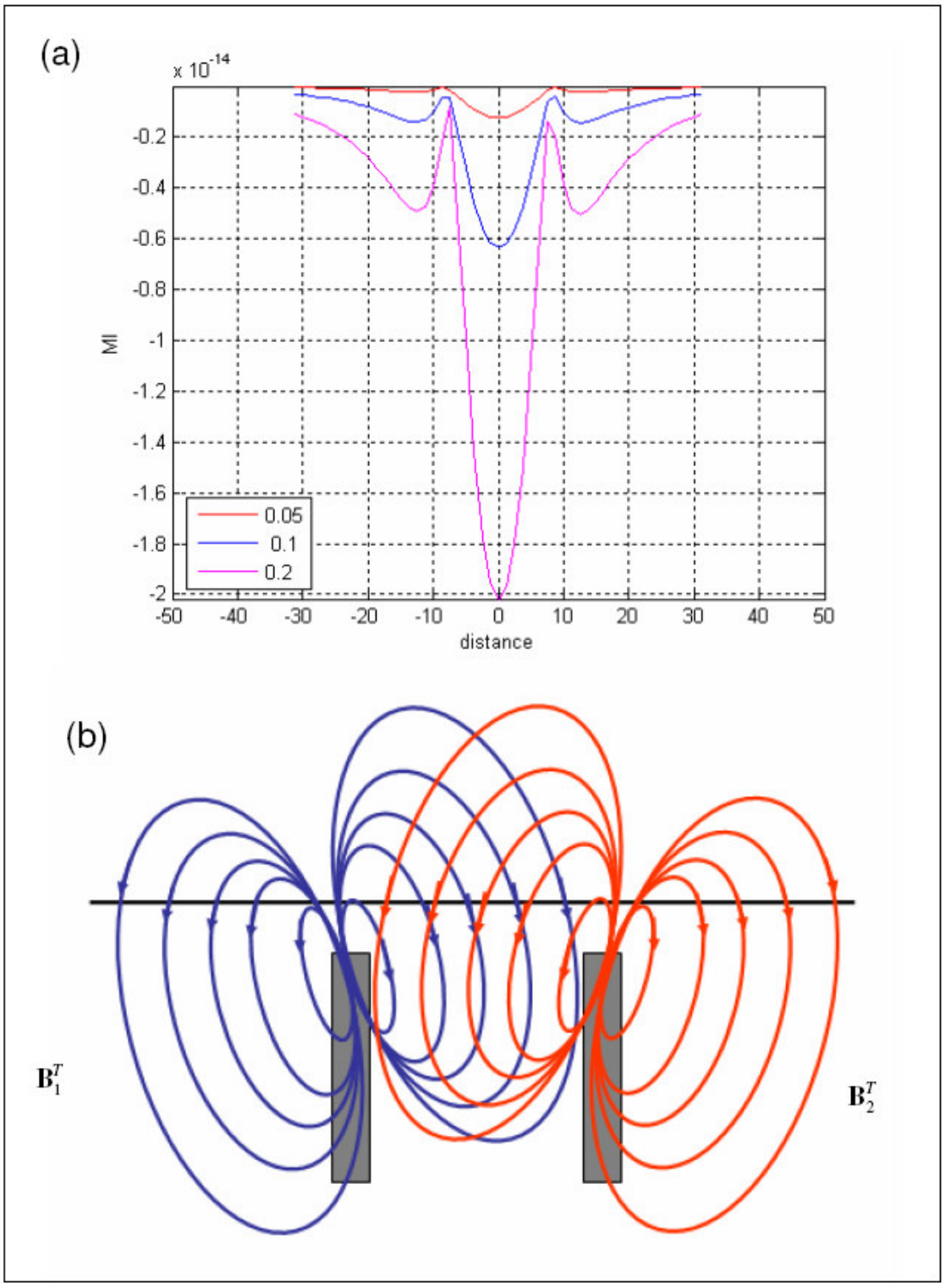

Figure 4.3. Mutual inductance (a) for model series A for frequency 1 KHz and orientation of tertiary currents (b).

by this current is shown in Figure 4.3. A similar process with generate a tertiary magnetic field in the left-hand slab, which is also shown in Figure 4.3. Using this theory, we can now explain the cause behind the main negative peak as seen in Figure 4.3 to be sum of the downward oriented tertiary field lines. From x = -30 to x = -13, the increase in the negative field is also attributed to an addition of the magnetic field lines oriented in the $-z$ direction. Also, there is an increase in density of field lines closer to the slab. The positive anomaly above the slab is due to the upward oriented field lines emanating from the slab.

Figure 4.5 is generated using the same models from Figure 4.3, but for a frequency of 10 KHz. The results are very similar to the previous case, with a higher MI effect seen in the case of slabs with higher conductivities. It is interesting to note that the pattern of the tertiary currents does not change with frequency, and simply appears to be scaled up. The tertiary fields again show a similarity to the field from a 2 dipole source as seen in the previous figure.

Figure 4.5 also shows the graph for MI vs distance for the same models discussed, but for a frequency of 20 KHz. As in the previous figure, the overall shape of the graph remains the same, with the main peak at zero position and two smaller peaks just beyond the slabs. The curves also reveal a trend of higher with higher frequency. The negative peak for the model with slab conductivity 0.2 S/m is ~ 4.2 x 10^{-13} Tesla. However, the graph also shows some amount of numerical noise beginning at an offset of 25 m from the source. This gives an indication of the code's degradation in performance at higher frequencies.

The H_z fields from the same models were calculated for mutual inductance for frequencies of 100 KHz and 500 KHz as well, and a high amount of numerical noise was seen. Based on this observation the frequencies selected for future models were chosen to be 0.5 KHz, 1 KHz and 2 KHz.

In addition to these a maximum MI vs frequency graph is presented in Figure 4.5 for slabs with different conductivity. The objective of this plot is to see how the tertiary currents change with increase in frequency. As seen in the previous graphs, the mutual

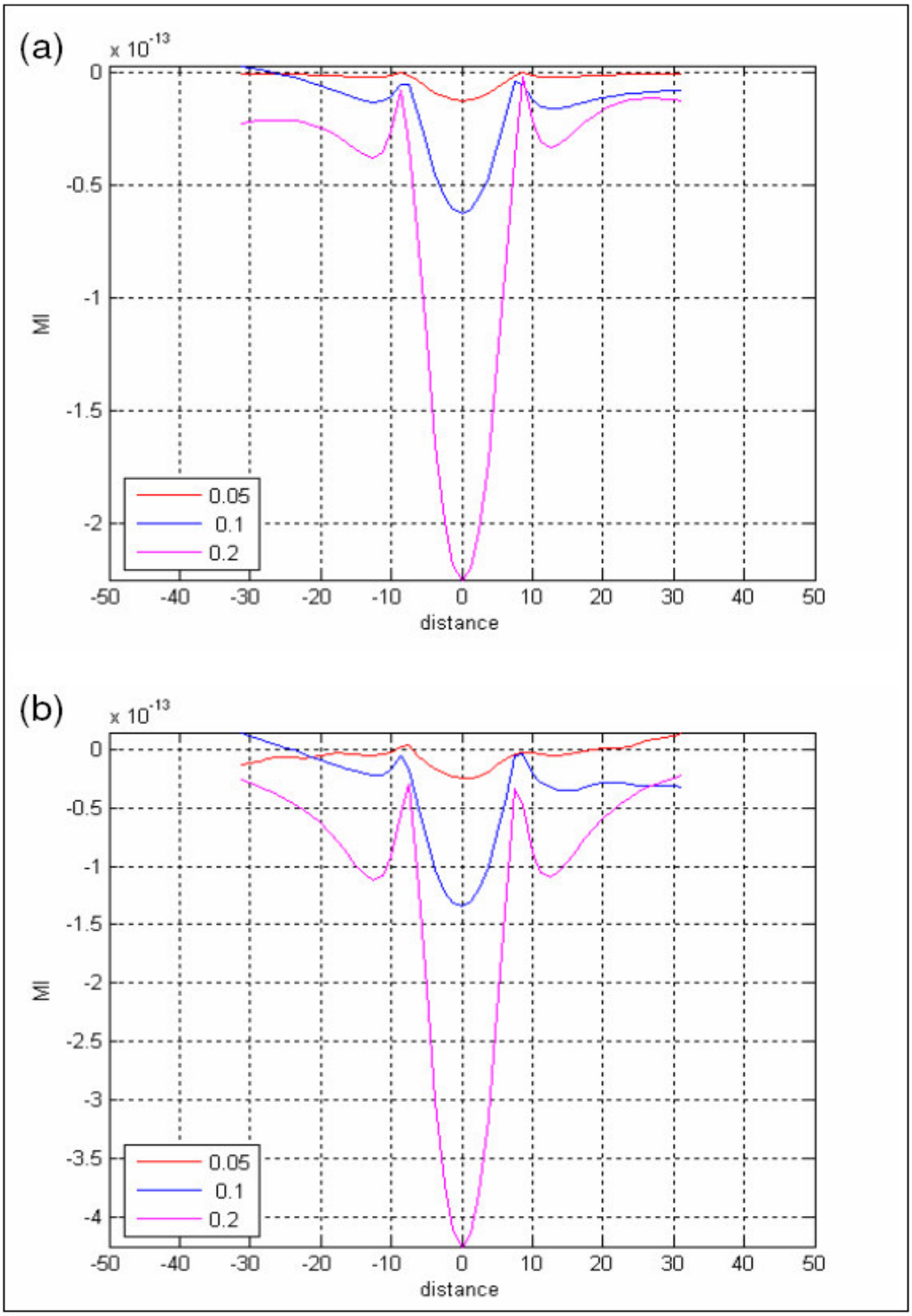

Figure 4.4. Mutual inductance for model series A for frequency (a) 10 KHz and (b) 20 KHz.

inductance is higher for targets with higher conductivities. From low to high frequencies the curve shows an increase in mutual inductance, implying a strong set of secondary currents generated in the targets. However, this trend is not expected to continue to very high frequencies due to the skin depth effect. Depending on the conductivity of the halfspace, at some higher frequency, the strength of the secondary currents generated in the targets will be very weak, which in turn will result in weaker tertiary currents.

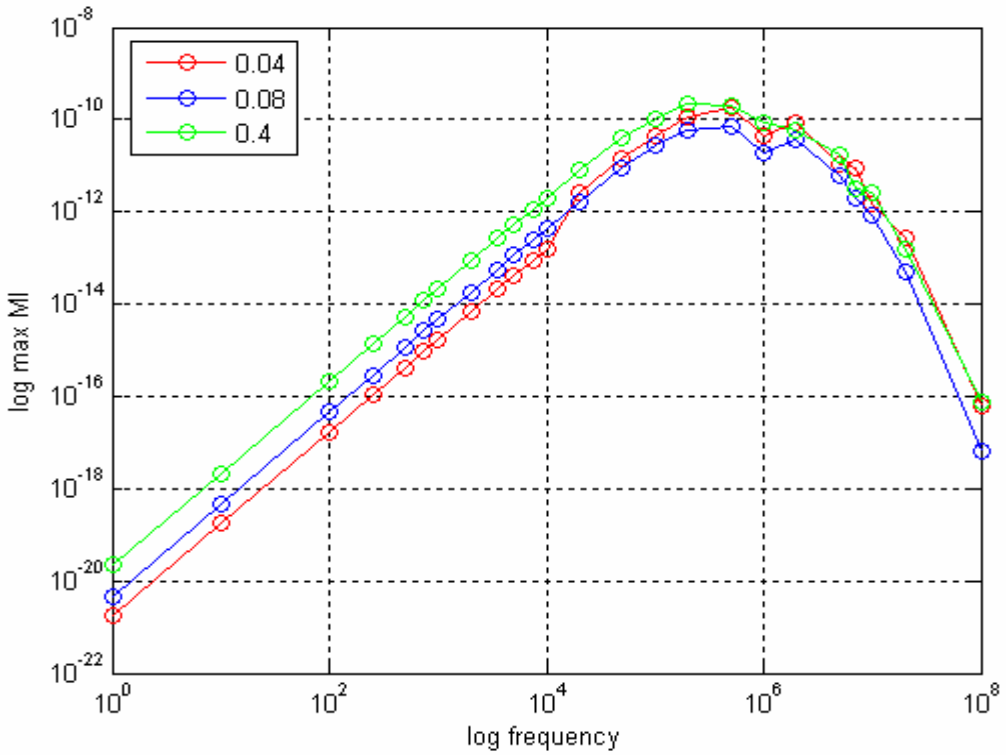

Figure 4.5. Max MI vs frequency for different slab conductivities in model suite A.

4.3. Model suite B

The mutual inductance for this suite has been calculated for a two slab model. The slabs are located on either side of the TX and are identical as far as dimensions are concerned. The difference between the two is the conductivity. The slab on the right-hand side has a fixed conductivity of 0.1 S/m while the left-hand slab conductivity varies from 0.1 S/m to 0.001 S/m to simulate a range of conductivities from fracture to metal.

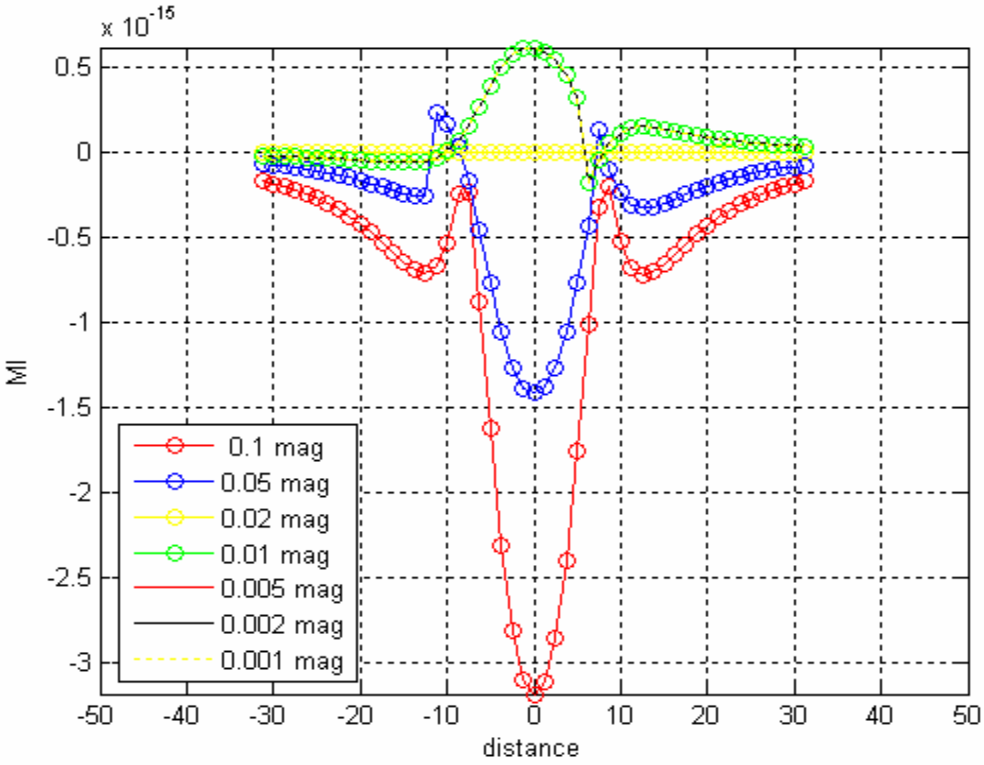

Figure 4.6. Mutual inductance for model series B for frequency 0.5 KHz.

Figures 4.6 shows the MI curves for the models for frequencies of 0.5 KHz generated by the tertiary fields shown in figure 4.7. Figures 4.8 shows similar MI curves for frequencies of 1 KHz and 2 KHz. In Figure 4.6 it is seen that when the left-hand slab has conductivity greater than the host, a negative MI peak is observed. For example, a peak is seen at -3.2 x 10^{-15} T when σ_L = 0.1 S/m. When the left-hand slab has conductivity lesser than the host, a positive MI peak is observed, *e.g.* when σ_L = 0.001 S/m a positive peak at 0.6 x 10^{-15} T is seen. To explain this change in sign, one must again turn to the effective conductivity of the slabs with respect to the host. Recall, for a resistive left-hand slab, the effective conductivity is negative, while for a conductive right-hand slab, the effective conductivity is positive.

First consider the case when the left-hand slab has a positive effective conductivity. In this case, the shape of the tertiary magnetic field lines emanating from the slabs will be the same as those seen in Figure 4.3 for model suite A. In fact, the case when σ_L = 0.1 S/m produces a MI curve that is identical in shape to those from model suite A. However, when σ_L = 0.05 S/m, the shape of the curve obtained is no longer symmetrical. There is a positive peak a little to the left of the left-hand slab, and a slight weaker positive peak above the right-hand slab. To explain this, consider the different conductivities in the slabs. The primary magnetic field fluxing through the slabs will induce a stronger set of secondary currents in the right-hand slab due to its greater conductivity. This in turn will induce a strong set of tertiary currents in the left-hand slab as compared to the right-hand slab. The positive peaks associated with the slabs are due to a tertiary magnetic field fluxing upward through a receiver located in the vicinity of the slab. The higher positive peak on the left side is due to the stronger H_z fields from the left-hand slab.

Now consider the case when the left-hand slab has an effective negative conductivity. The tertiary H_z fields for this model are shown in Figure 4.7. It is seen that in this case, the H_z fields between the two slabs is oriented upwards, which is the opposite of the case when effective conductivity of the left-hand slab is positive. To generate the field seen in Figure 4.7, the primary field fluxes downward through the

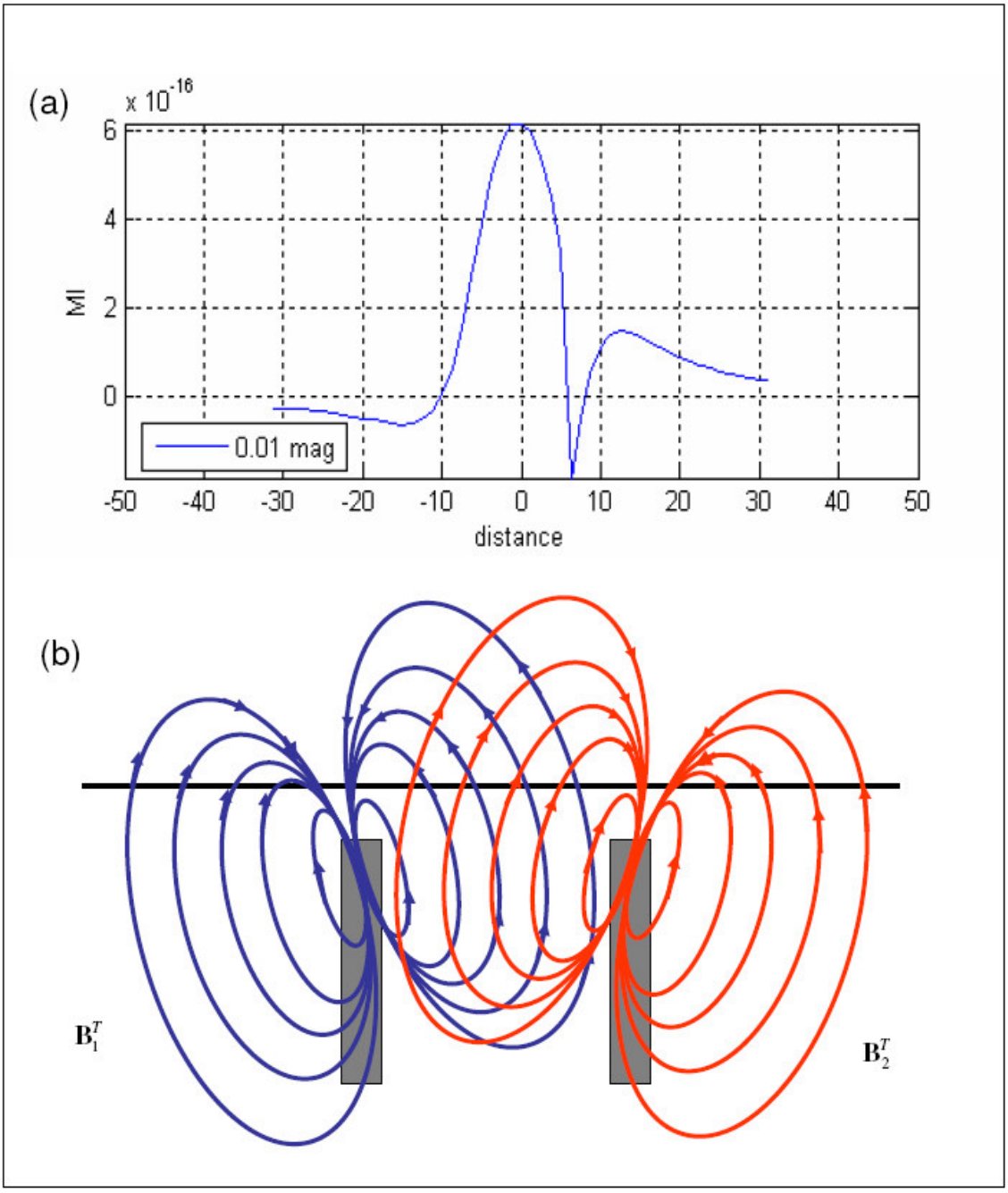

Figure 4.7. Mutual inductance (a) for model suite B when $\sigma_L < \sigma_{host}$ and tertiary fields (b) emanating from slabs for the same case.

left-hand slab, and is tilted to the left. The secondary currents induced by this fluxing field in the left-hand slab will not circulate in a clockwise direction, but in the opposite direction due to the effective negative conductivity, as seen in Figure 4.2. These currents will be slanted towards the right, and the secondary magnetic field lines due to these currents will flow upwards, tilted to the right. These currents will flux through the left-hand slab from right to left, and will be tilted downward. The tertiary currents due to this field will circulate in a clockwise direction and will be tilted to the right. These currents will produce the tertiary $\mathbf{B}_2^T(t)$ field shown in Figure 4.7. A similar induction process will occur as the primary magnetic field fluxes through the right-hand slab to generate a set of secondary currents, whose magnetic field will flux upward from right to left through the left-hand slab. The tertiary currents induced by this field are controlled by the effective negative conductivity of the slab, and the tertiary H_z field emanating from this slab is shown in Figure 4.7. The positive peak in between the two slabs is because of the tertiary currents fluxing upwards through the ground, between the two slabs. The sharp negative peak above the left-hand slab is due to a strong H_z field generated in the right-hand slab that fluxes downward.

Figure 4.6 also shows that for the case when $\sigma_L = \sigma_{host,}$ there is no mutual inductance, which is to be expected because effectively there is only one target in the halfspace.

Figure 4.8 shows the tertiary H_z fields from the same models but for frequencies of 1 KHz and 2 KHz. The overall shape of the curves is preserved in both these figures. However, with an increase in frequency there is an increase in magnitude of the tertiary currents. In fact, as the frequency doubles, the magnitude is also doubled. For example, consider the positive peak of the model with $\sigma_L = 0.01$ at $x \sim 0$. In Figure 4.8 (a), the magnitude of this peak is ~ 1.2 x 10^{-15} T at frequency I KHz, while it increases to 2.4 x 10^{-15} T with an increase in frequency 2 KHz as seen in Figure 4.8 (b).

From these figures, it is seen that the effect of increasing frequency is to simply scale the magnitude of the tertiary currents. It does affect the shape of the currents. Hence, for model suites C D and E, only plots for frequency 500 Hz will be presented.

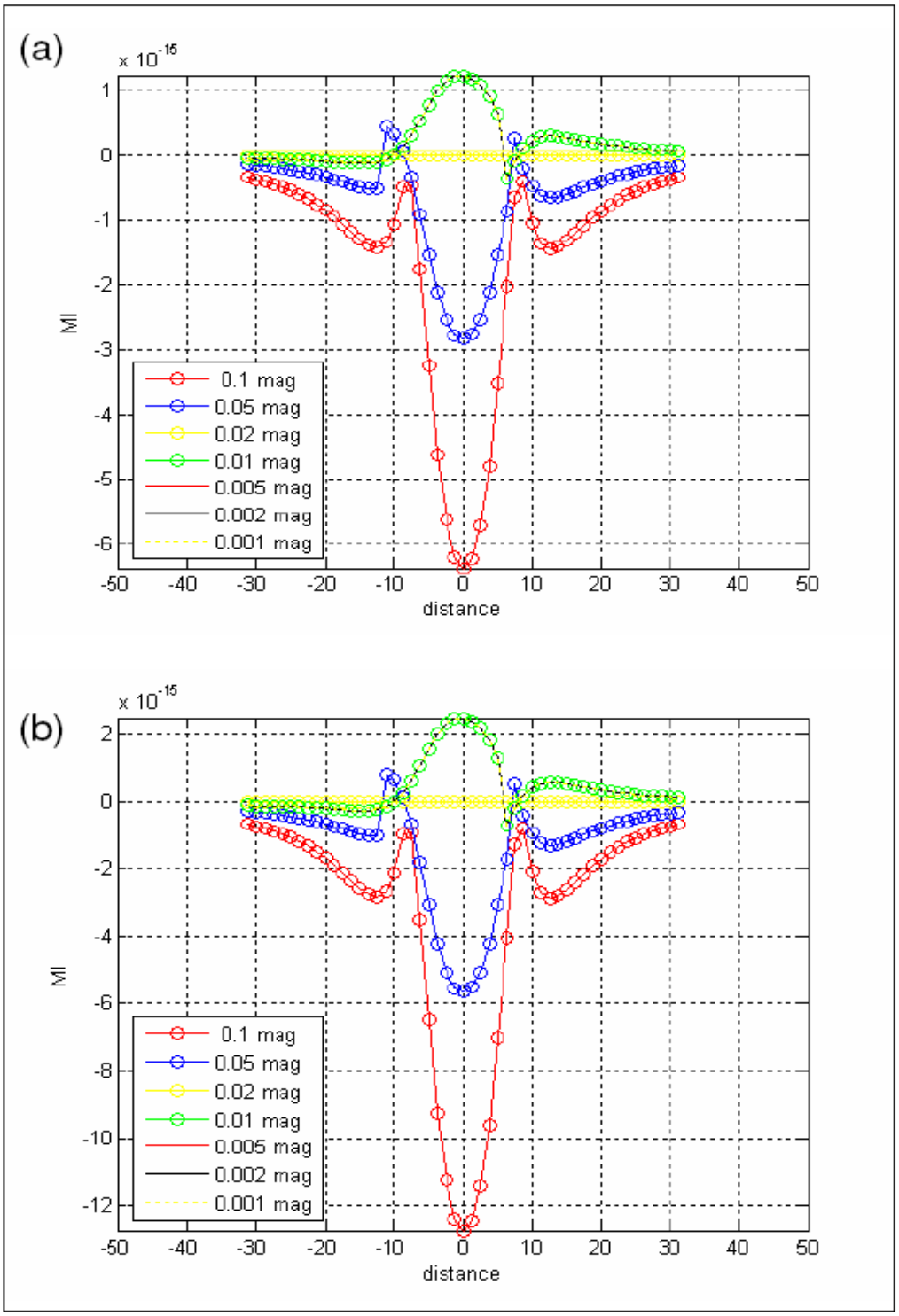

Figure 4.8. Mutual inductance for model series B for frequency (a) 1 KHz and (b) 2 KHz.

4.4. Model suite C

This model series takes a look at the effect of different TX positions on the tertiary currents. This is of significance in a profile type survey. To generate these graphs, a two slab model was used, with slab separation 10m. Both slabs are identical in terms of dimensions and conductivity. The graphs for 3 different TX positions relative to the slabs are presented in Figure 4.9 which shows the MI vs distance plot for frequency 0.5 Hz. The yellow curve is produced when the TX is located between the two slabs. This curve has been seen before in model series suite B. As expected, the curve is symmetrical about the TX due to the symmetry of the model.

The red colored curve in the figure is obtained when the source is located 5 m to the left of the left-hand slab. The tertiary field lines for the slabs from this model are presented in Figure 4.10 (c). This figure also shows the primary magnetic field $\mathbf{B}^{P}(t)$ fluxing through the slabs. While this field fluxes downward through the left-hand slab, it fluxes upward through the right hand slab. This plays a very important role in determining the orientation of the secondary currents and therefore the tertiary field. Secondary currents developed in the left-hand slab will be flow in a clockwise direction, and will be tilted to the left. The secondary magnetic field from this slab will flux through the right-hand slab from in the $-z$ direction from right to left. This will induce a set of tertiary currents in the right-hand slab that will circulate in a counter clockwise direction and will produce a tertiary H_z field as seen in Figure 4.10 (c). To produce the other set of tertiary currents, the primary field fluxes upwards through the right-hand slab from left to right, and will induce a set of secondary currents that circulate in a counter-clockwise direction and is tilted to the right. The secondary magnetic field from these currents will flux through the left-hand slab from right to left and will point downward. This induces a set of tertiary currents in the left hand slab that circulate in a clockwise direction and is tilted to the right. The tertiary H_z field emanating from this slab is shown in Figure 4.10. It is important to recognize the difference in the magnitude of the tertiary currents produced due to the location of the TX. Since the source is closer to the left hand slab, the secondary currents will be stronger in the left-hand slab as

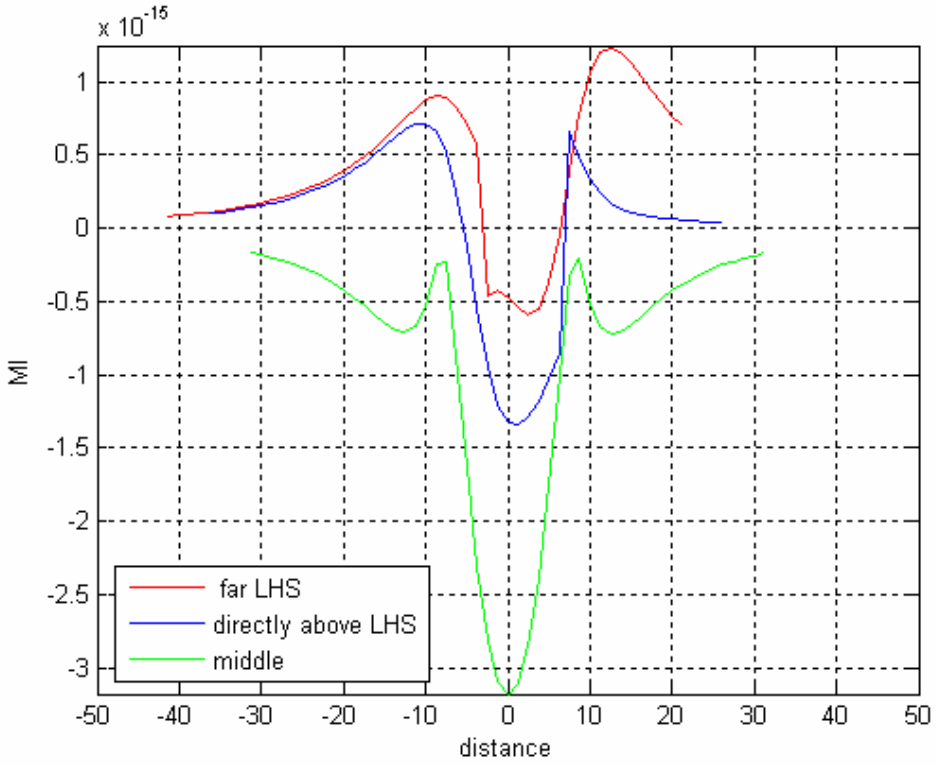

Figure 4.9. Mutual inductance for model series C for frequency 0.5 KHz.

compared to the right-hand slab. This will produce a stronger set of tertiary currents in the right-hand slab as compared to the left-hand slab. In fact, the tertiary field from the right-hand slab is strong enough to cause a negative anomaly in between the slabs even though the field from the left-hand slab is oriented upwards in this region. The stronger tertiary magnetic field from the right-hand slab will cause a high the positive anomaly on the right-hand side.

When the TX is located directly above the left-hand slab, the MI has a positive peak above the left-hand slab, and a higher positive peak above the right-hand slab, as depicted by the blue curve. An anomaly in this curve is the sharp *horn* located at $x \sim 7$ m in the blue peak representing the case when the TX is located just above the right-hand

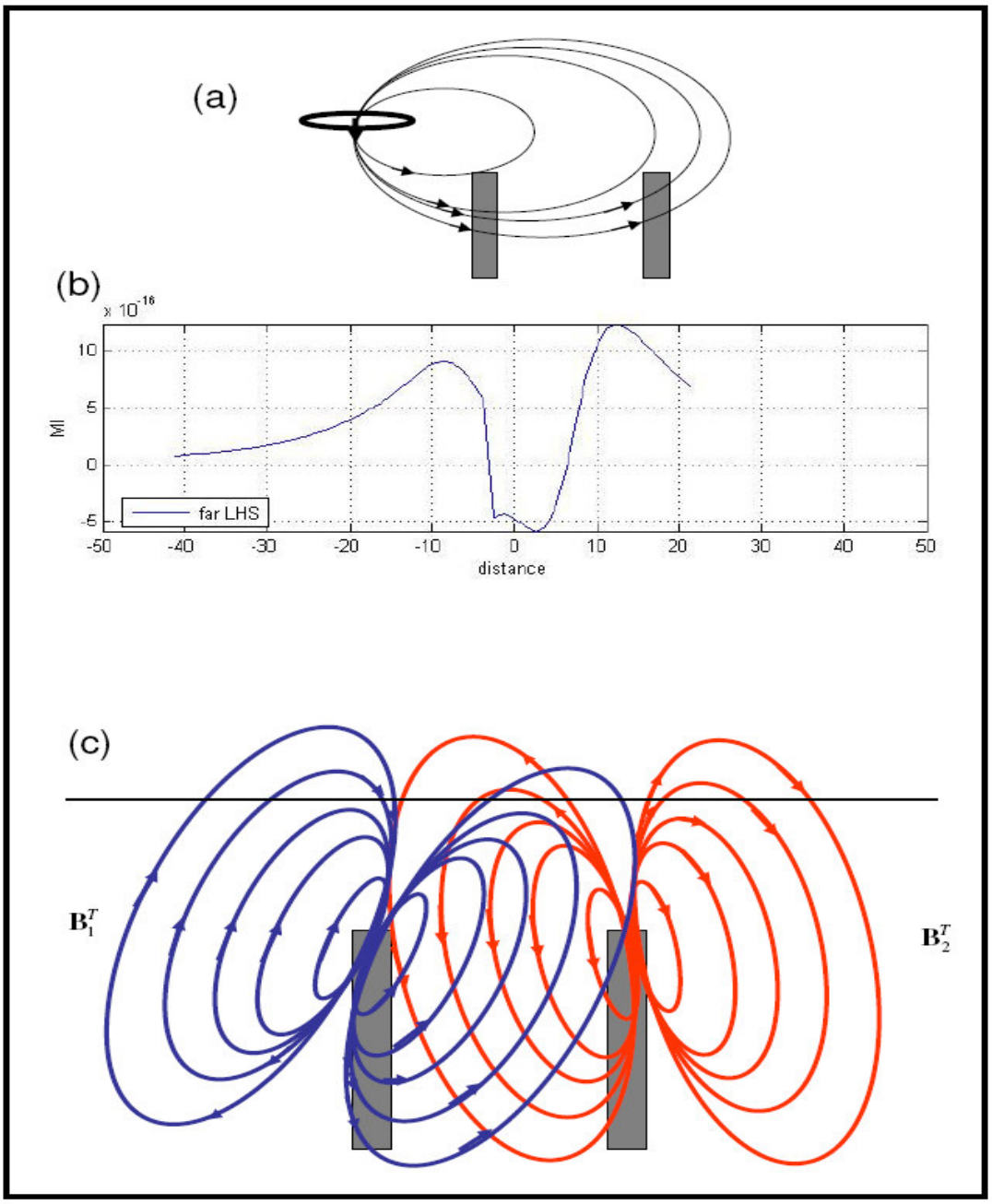

Figure 4.10. (a) Primary magnetic field $\mathbf{B}^P(t)$ fluxing through slabs to develop tertiary response (b) due to tertiary field (c) when source is away from both slabs.

slab. This *horn* is characterized by sharp rise on one side and a vertical rise on the other. The tertiary H_z field lines for this model are presented in Figure 4.11 (c).

Figure 4.11 (a) shows how the primary magnetic field from the source fluxes through the slabs. When the TX is located above the left-hand slab, the field lines flux vertically through the slab. This will generate a set of secondary currents that will circulate in a clockwise direction and will be horizontal. The left-hand slab then acts as a secondary horizontal magnetic dipole (HMD), and the field lines from this secondary source will flux vertically through the right hand slab. This is due to the relative orientation of the two slabs. The right-hand slab will act as a tertiary HMD that is oriented in the $-z$ direction. The primary field will flux through the right-hand slab from left to right, in a downward direction. Secondary currents induced by this field will circulate in a clockwise direction, and are tilted to the left. The secondary H_z field from these currents will flux upward through the left-hand slab from right to left and will induce a set of tertiary currents. The tertiary magnetic field due to these currents is shown in Figure 4.11 (c). Regarding the magnitude of these fields, the tertiary H_z field from the left-hand slab will be stronger than the right-hand slab because a stronger set of secondary currents is induced in the right-hand slab. Due to the low surface area of the top of the slabs, a lower number of primary magnetic field lines will flux through the left hand slab. The strong negative peak in between the two slabs is due to the H_z field oriented in the z direction from both slabs in this region. The upward pointing H_z field in the region surrounding the left-hand slab will result in the positive anomaly seen in figure 4.11. One of the unique aspects of this model suite is the development of the *horn* above the right-hand slab, which is not seen in any other model thus far. This is attributed to the location of the TX directly above the left-hand slab, which causes the right-hand slab to act as a tertiary HMD. In order to get a better insight into the development of this horn, four more TX locations were added to this model. Thus, the H_z field for a total of 7 TX locations has been calculated, and the mutual inductance for these models is shown in Figure 4.12. Here too the horn is generated only when the TX is above the left-hand slab. This is an important observation because if this horn is

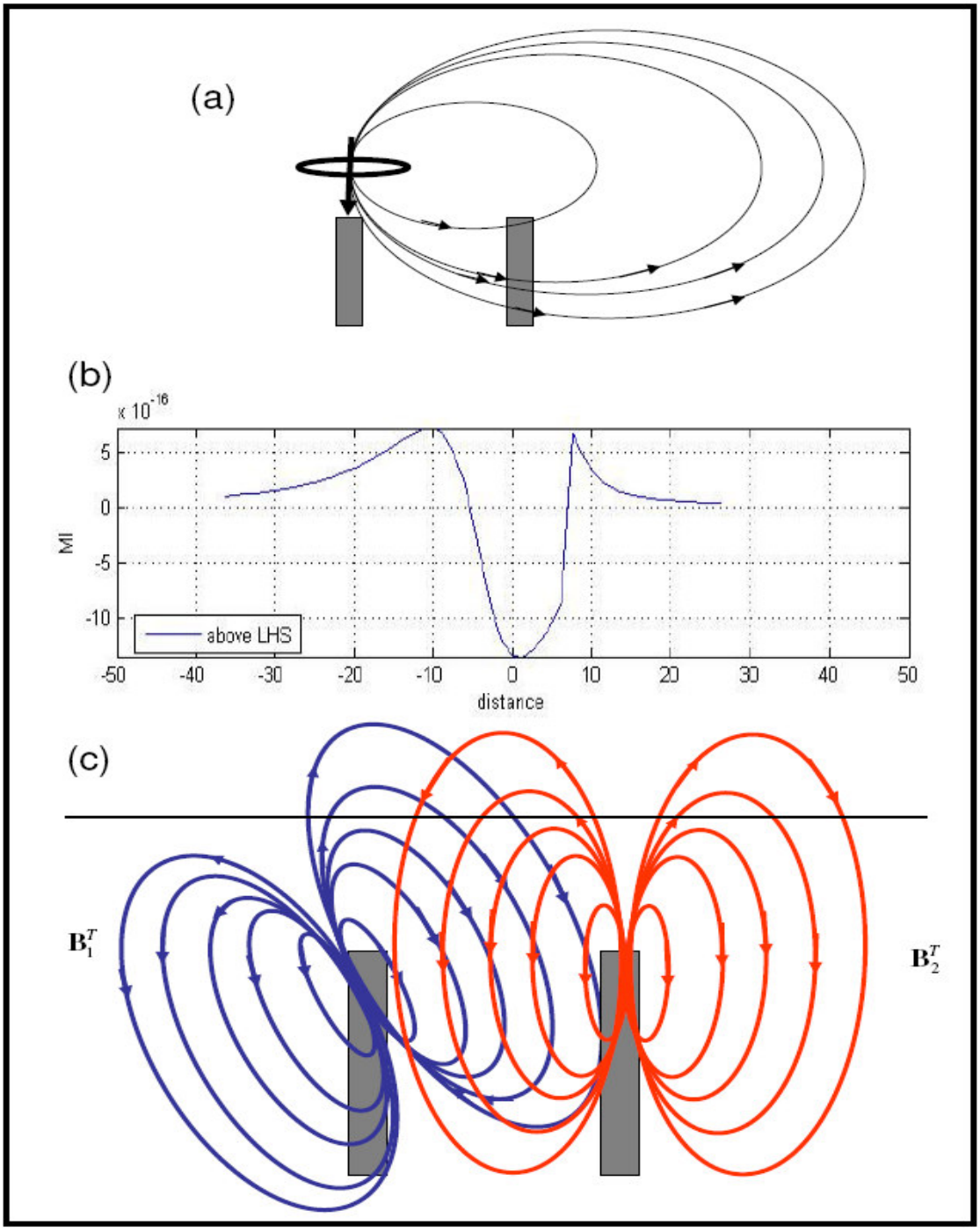

Figure 4.11. (a) Primary magnetic field $\mathbf{B}^P(t)$ fluxing through slabs to develop tertiary response (b) due to tertiary field (c) when source is directly above left-hand slab.

observed in field data, it might indicate that there are two conductive heterogeneities, one below the RX location at which the horn is observed, and another beneath the TX location.

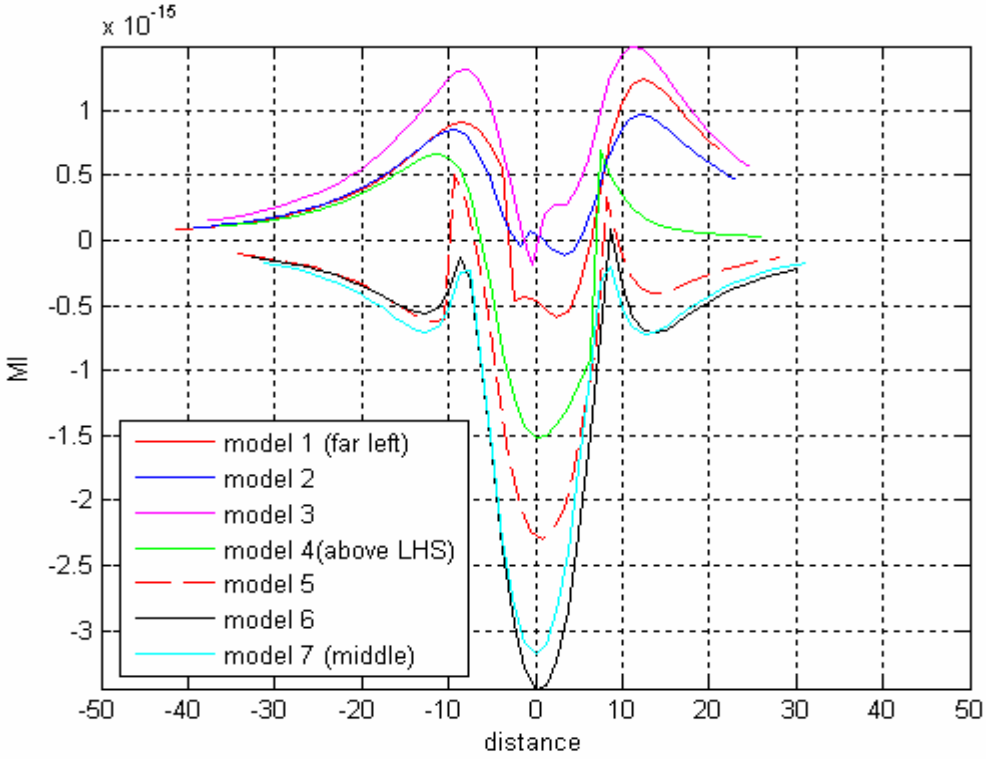

Figure 4.12. Mutual inductance for model suite C, with 7 TX positions.

4.5. Model suite D

In this model suite, I study the effect of TX position on the H_z field from a conductive target and a metal slab. Again, the two slab model is used, but left-hand slab conductivity σ_L = 0.05 S/m and right-hand slab conductivity σ_R = 0.1 S/m. Five different TX positions have been selected, on the far left and right hand sides, above each slab, and in between the two slabs. Figure 4.13 shows the curves for the five TX locations for frequency of 500 Hz. First consider the curves produced when the TX is located away from both slabs. The red curve, produced when the TX is located 5 m to the left of the left-hand slab has two positive peaks, corresponding to each of the slabs and a sharp negative peak associated with the right-hand slab. The positive peak on the right side is higher than the peak on the left side. There are two reasons why this occurs. Because the left-hand slab is closer to the TX, it will have a higher set of secondary currents in it, and will therefore induce a strong tertiary field in the right-hand slab. Also, the right-hand slab is twice as conductive as the left hand slab and will therefore be able to sustain stronger tertiary currents which cause the higher peak. A similar phenomenon is seen in the green curve, produced when the TX is located to the 5 m to the right of the right-hand slab. In this case also, the TX is located away from both slabs. this curve is a mirror image of the tertiary fields from the previous location. The positive peak on the left side is higher than the peak on the right side. This may be attributed to a stronger set of secondary currents in the right hand slab due to its proximity to the TX and due to its high conductivity. It therefore acts as a very strong source of tertiary currents to the left-hand slab. The lower positive peak on the right hand side is due to the comparatively weaker set of secondary currents induced in the left-hand slab by the TX.

The blue curve in the figure represents the tertiary H_z field when the TX is located directly above the left-hand slab, while the black curve represents the tertiary H_z field when the TX is located directly above the right-hand slab. Both these curves show a sharp *horn* associated with the slab on the opposite side of the TX. There is a smooth positive peak on both curves associated with the slab directly beneath the TX. It is interesting to note that for both TX locations, the peak on the right side is higher than the

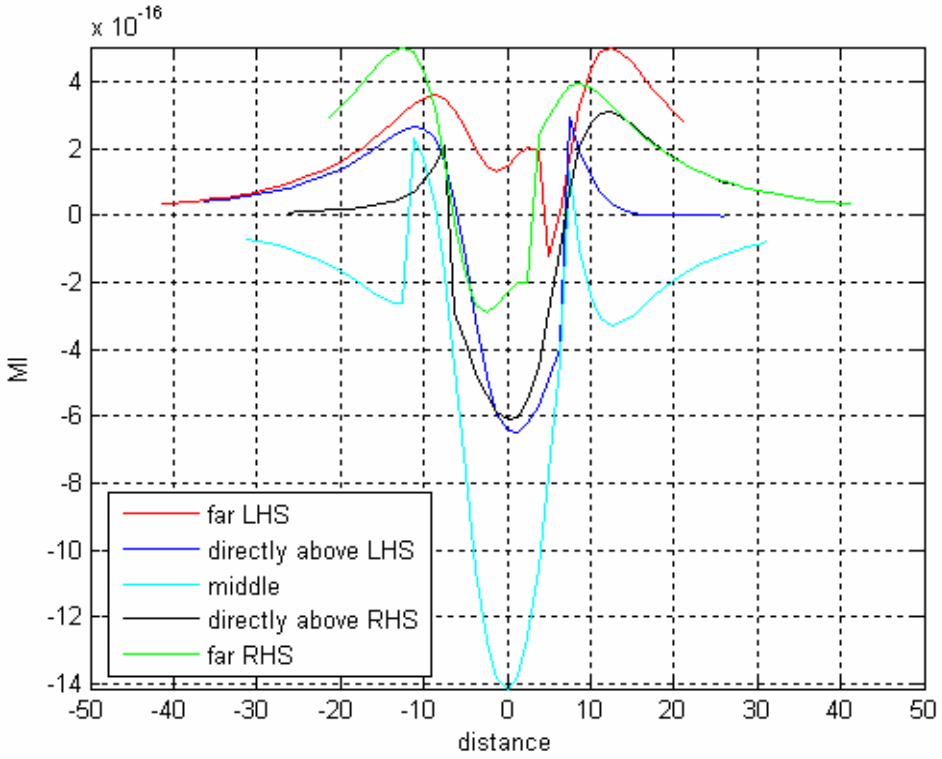

Figure 4.13. Mutual inductance for model suite D, frequency = 0.5 KHz.

peak on the left side. As in the previous model suite, the formation of the horn is due to the slab acting as a horizontal magnetic dipole. First consider the blue curve representing the TX location above the left-hand slab. In this case, the left-slab will have a greater set of secondary currents than the right-hand slab, which will contribute to a stronger set of tertiary currents in the right-hand slab. This will cause a higher peak on the right-hand side. The positive peak in the black curve representing TX location above the right-hand slab has a slightly different explanation. In this case, the right-hand slab will have a much stronger set of secondary currents which will induce a very strong set of tertiary currents in the left-hand slab. However, the lower conductivity of the left-hand slab will not be able to sustain as much current as the right-hand slab. Therefore, despite the fact that the left-hand slab acts as a comparatively weaker source of tertiary currents to the

right-hand slab, the higher conductivity of the right-hand slab will provide a better response to induction from the secondary field, resulting in a higher peak. The cyan colored curve in Figure 4.13 represents the case when the TX is located in between the two slabs. This curve has a strong negative peak at location x=0 which may be attributed to the symmetry of the model. Two smaller negative peaks on either side of this strong negative peak are seen, with a stronger peak on the right-hand side. This may be attributed to a strong response of the more conductive right-hand slab to the secondary currents from the left-hand slab. This curve also shows the formation of the *horn* on the right and left hand side.

4.6. Model suite E

This model looks at the mutual inductance between a metal slab on the left-hand side and a resistive slab on the right-hand side for different TX positions. Five TX locations have been selected for this model, which are the same as those selected for model suite D. The mutual inductance for these models for a source with frequency 0.5 KHz is presented in Figure 4.14. The conductivity of the left-hand slab is 0.01 S/m while that of the right-hand slab is 0.1 S/m.

What sets these results apart from the previous two model suites is that while suites C and D are dominated by strong negative peaks around location $x = 0$, the curves for this model suite are dominated by a strong positive around the same location. An analogy to this situation may be seen with respect to model suite B, where a resistive ($\sigma_{slab} < \sigma_{host}$) and conductive ($\sigma_{slab} > \sigma_{slab}$) left-hand slab showed opposite MI peaks in the presence of a conductive slab on the right-hand side. This is due to the sign difference in the effective conductivity of the slabs, which cause secondary currents in a slab with negative effective conductivity to circulate in a direction opposite to the case of a slab with positive effective conductivity, as seen in figures 4.2. Keeping this in mind, the effect of the negative conductivity will be to produce a positive peak

A strange characteristic of this model suite is that the for the red curve, produced for a TX located at the far left of the model, is very similar to the curve produced by the

same TX location in the previous models. The area in between the two curves is still dominated by a negative anomaly. This is the only model in this suite for which the anomaly in the middle is negative. Another strange phenomenon in this model suite is that when the TX is directly above the right-hand conductive slab, there is no horn developed above the left-hand slab. Thus I conclude that the horn is developed only over a target that has an effective positive conductivity.

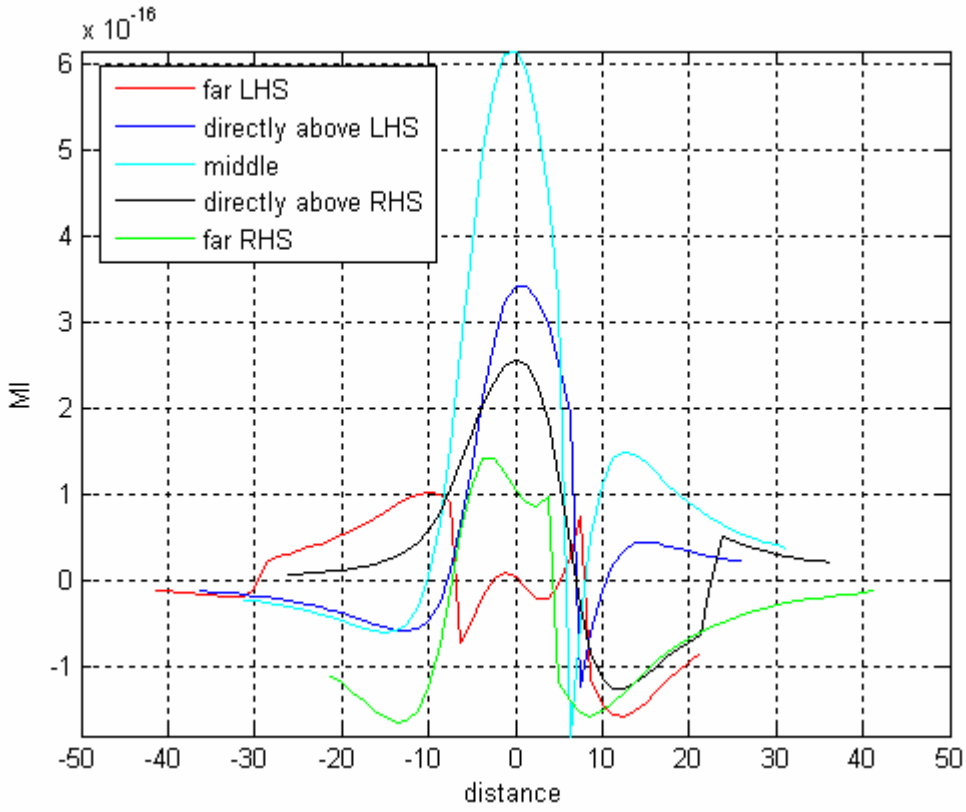

Figure 4.14. Mutual inductance for model suite E, frequency = 0.5 KHz.

4.7. Model suite F

This model series analyses the tertiary H_z fields from two slabs of different shape or orientation. Three models are presented here, in which both slabs have same conductivity. The right-hand slab for the models is identical to the right-hand slab from previous models and has a conductivity of 0.1 S/m. The left-hand slab varies in shape and orientation.

Figure 4.15 shows the tertiary H_z field for model series 1 of this suite, in which the left hand slab is horizontal, with a conductivity of 0.1 S/m. Dimensions of the slab are 5 m x 10 m x 1.25 m in the *x, y* and *z* directions respectively. The depth to the top of both right and left-hand slabs is 5 m. The red, blue and magenta curves in the figure represent the results for three frequencies of 500 Hz, 1000 Hz and 2000 Hz. These curves have a high negative peak at position x~ -3, which is flanked by a lower negative peaks on either side at locations x ~ -13 and x ~ 13. Among the lower negative peaks, the peak on the right side has a greater magnitude. There are two sharp positive peaks separating the negative peaks. In order to understand the shape of the tertiary current developed in this model, let us first look at the primary field fluxing through the slabs. Due to its greater surface area at the top, the left hand slab will accommodate a greater number of magnetic field lines through its upper surface. This will induce a series of secondary eddy currents in the slab that will circulate in the clockwise direction, but due to orientation of the slab, these currents will be slightly tilted to the right. The secondary magnetic field induced by these currents will flux upward through the right-hand slab, from left to right. The tertiary currents developed in the right-hand slab will circulate in a counter-clockwise direction and will be tilted slightly to the right. The tertiary magnetic field lines emanating from this slab are presented in Figure 4.15. A similar induction process will result in a series of tertiary currents induced in the left-hand slab. It is important to recognize that in this model series, the orientation of the tertiary currents is controlled by the shape of the slabs. The tertiary magnetic field from the left-hand slab is more inclined than the field from the right-hand slab. Also, the secondary field from the left-hand slab is stronger than that of the right-hand slab, which will cause

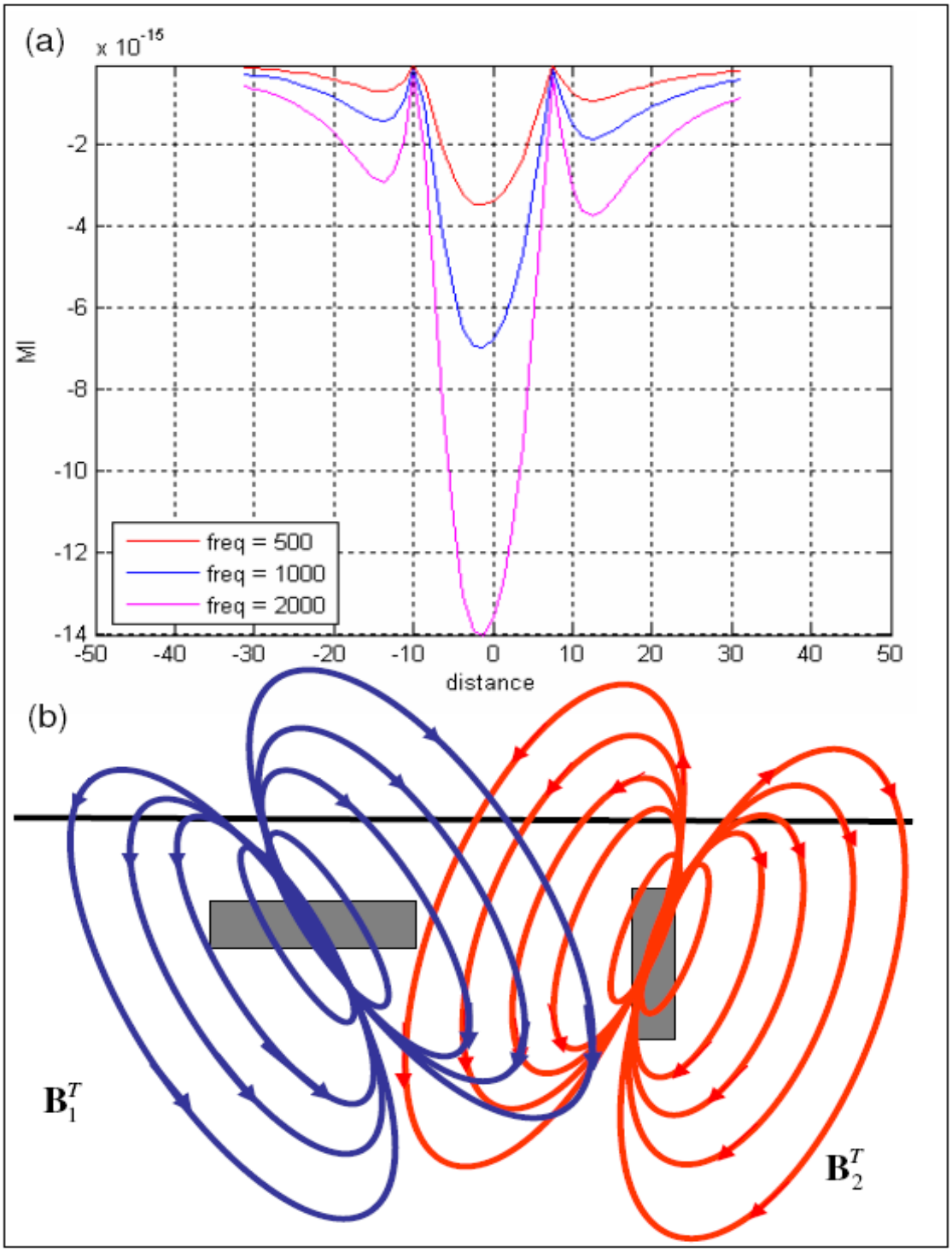

Figure 4.15. Mutual inductance (a) for model suite F, with horizontal left-hand slab and associated tertiary magnetic (b) field lines emanating from slabs.

a stronger tertiary field in the right-hand slab. This results in a higher negative anomaly associated with the left-hand slab. The offset of the main negative peak in between the two slabs is interpreted to be due to the stronger tilt in the tertiary magnetic field from the left-hand slab.

The tertiary H_z field for model series 2 of this suite, with a longer left-hand slab is shown in Figure 4.16. The left-hand slab in this case has a height of 10 m, and a length of 1.25 m and 10 m in the x and y directions respectively. As in the previous case, the red, blue and magenta curves in the figure represent the results for frequencies 500 Hz, 1 KHz and 2 KHz respectively. The plots show a strong negative peak at $x = 0$, which indicates that the orientation of the tertiary fields in both slabs are symmetrical. However, it is seen that among the two smaller negative peaks located at x ~ -13 and x ~ 13, the peak on the left-hand side is stronger. These curves are similar to the curves obtained from model suite A. The only difference the two is that the negative peak on the left-hand side is smaller than the negative peak on the right-hand side. The orientation of the tertiary fields from this model will be the same as those from model suite A. However, the field from the right and left-hand slabs will differ in magnitude. Since the height of the left-hand slab is double that of the right hand slab the number of magnetic field lines fluxing through the left-hand slab is much greater than the right-hand slab. The left-hand slab will therefore have a stronger tertiary magnetic field because it is able to sustain more tertiary current than the right-hand slab. This will cause the left-hand peak to be stronger than the right-hand peak. The main negative at $x = 0$ further supports the idea that the shape and orientation of the tertiary field from both slabs is symmetrical.

Figure 4.17 shows the tertiary H_z field for the case when the left-hand slab is a cube with conductivity 0.1 S/m and length 2.5 m. The cube is buried so that depth to the top of the cube is 5 m, which matches that of the right-hand slab. The graph for this model shows a strong negative peak close to $x = 0$, but slightly offset to the left, closer to the cube. The graph also shows a strong smooth positive peak to the left of the cube, and a sharp positive peak above the right-hand slab. Also associated with the right-hand

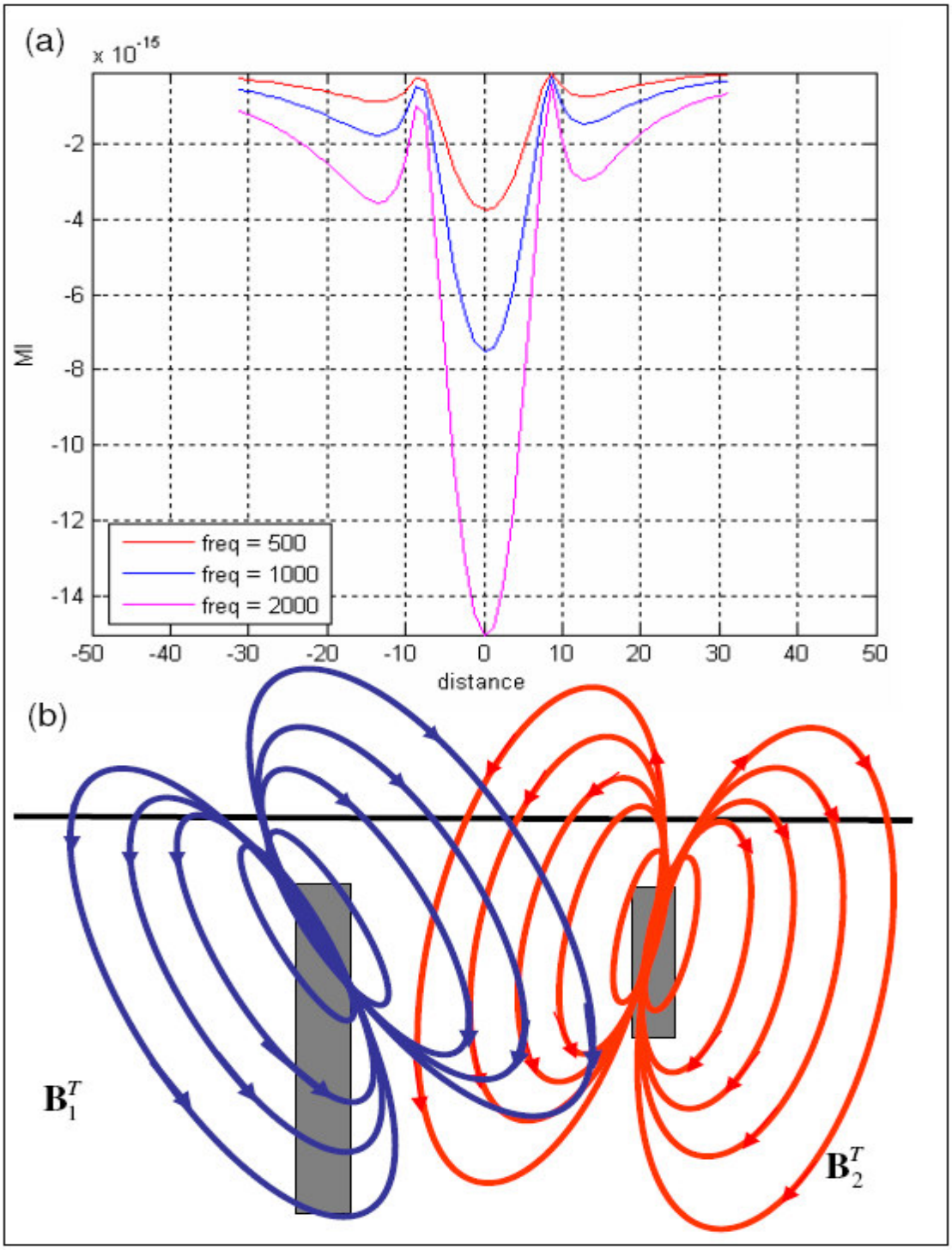

Figure 4.16. Mutual inductance (a) for model suite F, with longer left-hand slab and associated tertiary magnetic (b) field lines emanating from slabs.

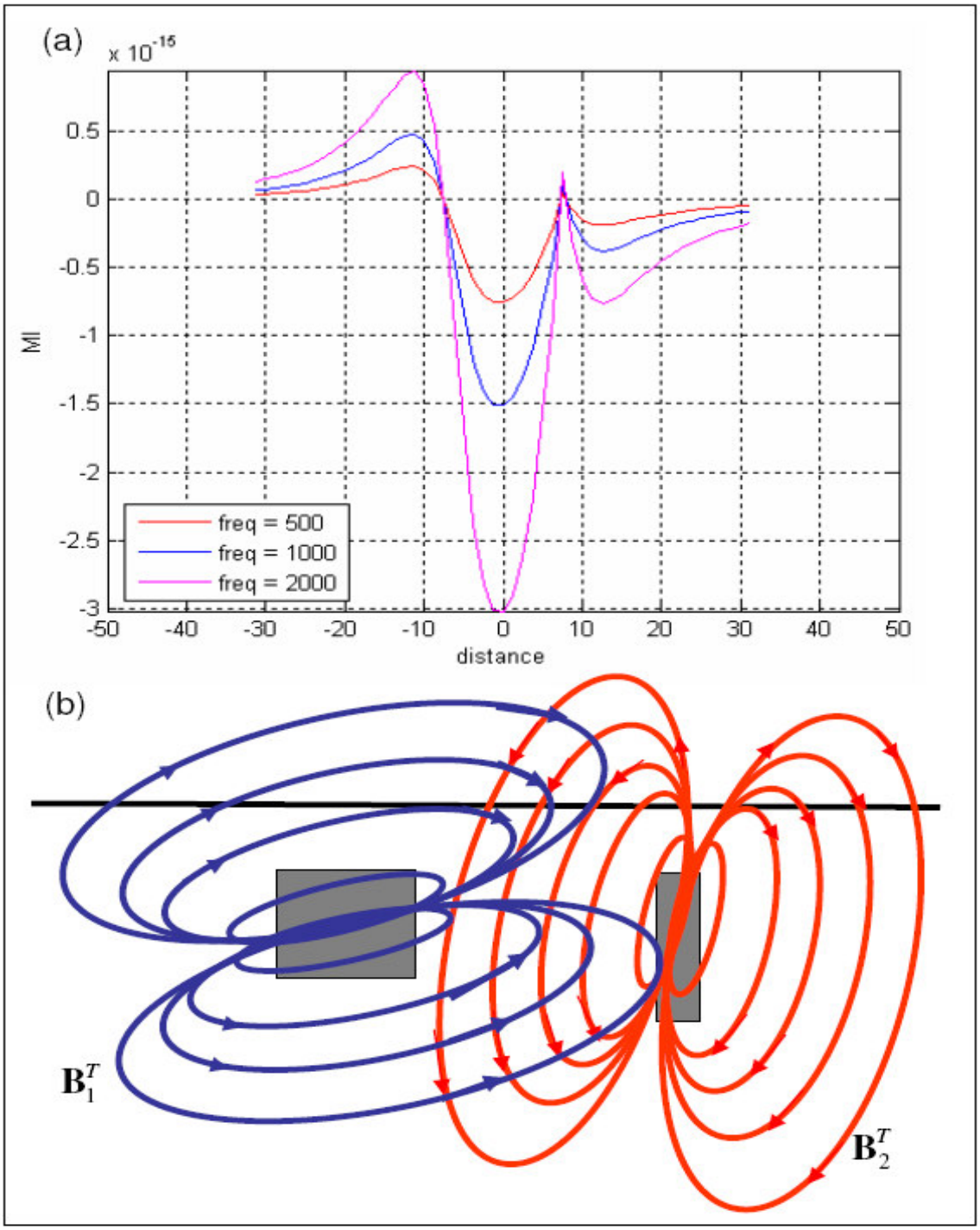

Figure 4.17. Mutual inductance (a) for model suite F with cubic left-hand slab and associated tertiary magnetic (b) field lines emanating from slabs.

slab is a negative peak which is approximately three times smaller than the main negative peak. What is interesting to note for this model is that the H_z field above the left and right-hand slabs is zero. Based on the shape of the curves in figure, it appears that the tertiary magnetic field from the left-hand slab is that of a nearly vertical magnetic dipole, and is oriented in the $-x$ direction; the field from the right-hand slab, on the other hand is that of a nearly horizontal magnetic dipole, oriented upwards. These field lines are shown in Figure 4.17 (b).

4.8. Model suite G

The three models in this suite are similar to the models in model suite F, the difference between the two is that while in the previous model suite, the left-hand slab has a conductivity of 0.1 S/m, this model suite has a left-hand slab conductivity of 0.05 S/m. The left-hand slab is therefore conductive with respect to the host conductivity. An interesting feature of this model suite is that the shapes of the tertiary H_z curves for this model are identical to those from the previous model, the difference between the two sets of plots being the magnitudes of the H_z field. For this model suite, the tertiary magnetic fields have a lower magnitude than the previous suite. Thus, the shape and orientation of the tertiary magnetic field lines from this model suite are the same as those seen in model suite F.

Figures 4.18 (a) and (b), and 4.19 show the mutual inductance for model series 1, 2 and 3 respectively for this suite. The red, blue and magenta curves in the figure represent the tertiary H_z fields for three frequencies of 500 Hz, 1000 Hz and 2000 Hz. The lower magnitude for H_z fields from this model suite is attributed to the lower conductivity of the left-hand slab. In this case, the tertiary field induced in the left-hand slab will be weaker as compared to the previous model suite. Also, the secondary field induced in the left-hand slab will be weaker than that induced in model suite F, which will result in the induction of weaker tertiary currents in the right-hand slab. When compared to the previous model suite, the tertiary magnetic fields emanating from both slabs are weaker in this suite.

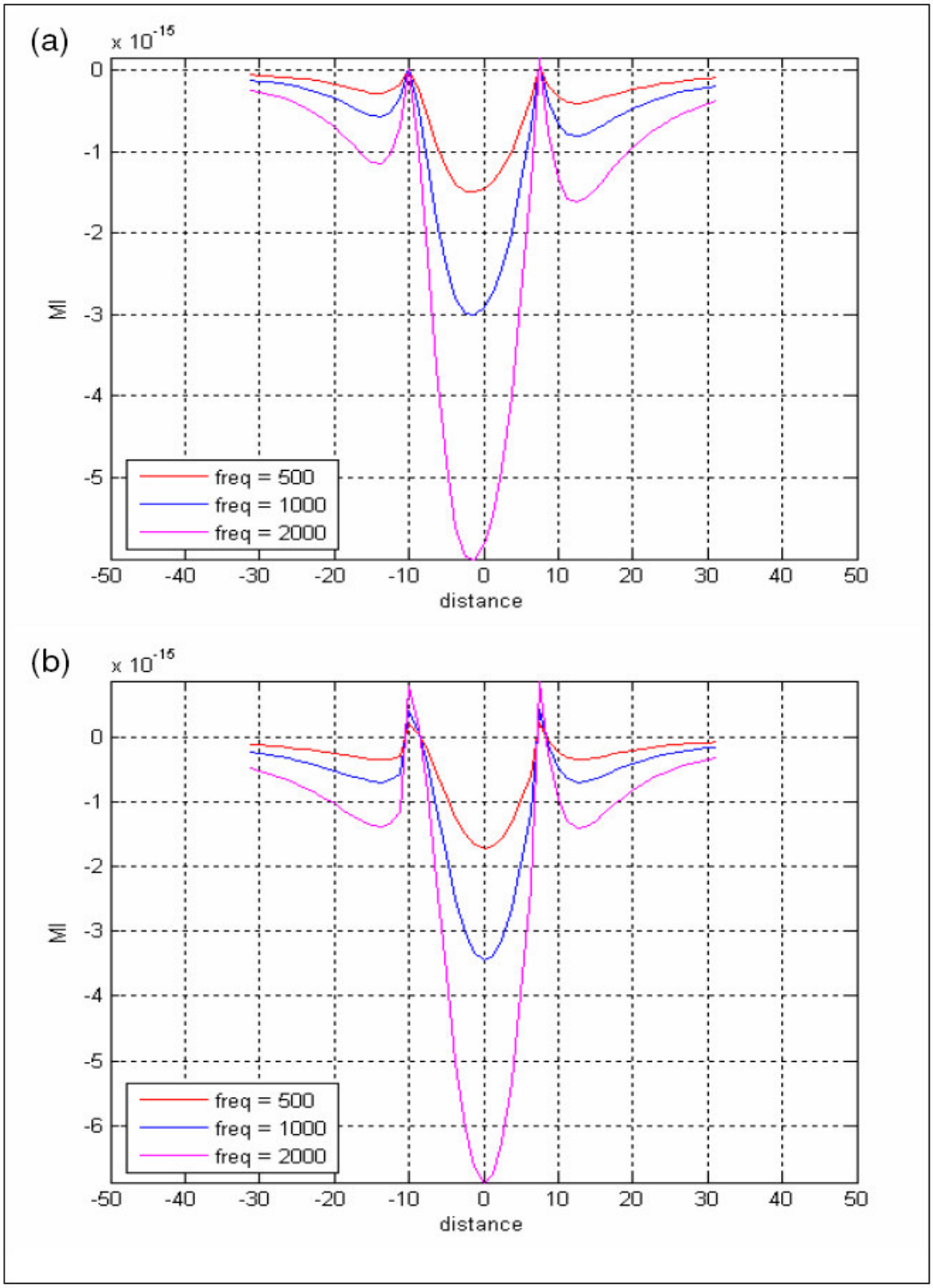

Figure 4.18. Mutual inductance for model suite G, (a) left-hand horizontal slab and (b) left-hand vertical slab.

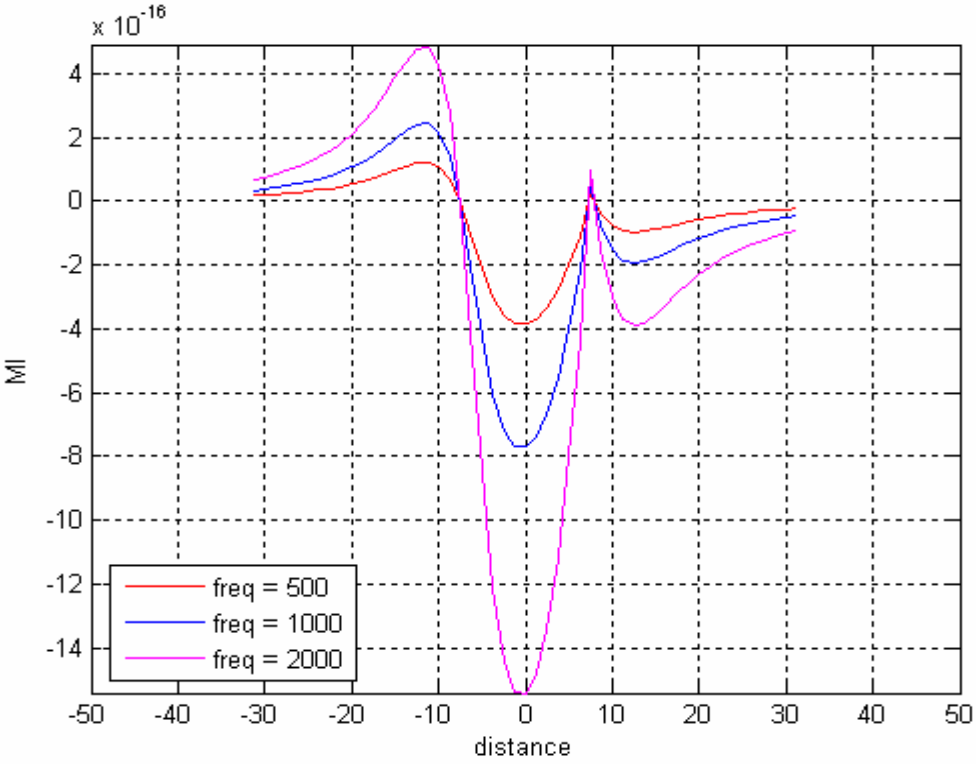

Figure 4.19. Mutual inductance for model suite G, cubic left-hand slab.

4.9. Model suite H

This model suite simulated the tertiary currents resulting from the mutual coupling between a resistive target on the left-hand slab with conductivity 0.01 S/m, and a cultural conductor on the right-hand side with a conductivity of 0.1 S/m. The shapes of the left-hand slab are the same as those of the previous two models. The results for these models are presented in Figures 4.20, 4.21 and 4.22.

Figure 4.20 shows the curve for the tertiary H_z field from a model that uses a horizontal left-hand slab for frequencies of 0.5 KHz, 1 KHz and 2 KHz. In this case, there is a very sharp negative peak at $x \sim 7.5$ There are two positive peaks on either side of this anomaly at locations $x = 2.5$ and $x = 12.5$, with the left-side peak stronger than the right. The tertiary *Hz* field in this case is very similar to that of a vertical magnetic dipole positioned at the location of the right-hand slab, oriented downwards. On the left-hand side, at x ~ 7.5, there is a very slight bump in the mutual inductance curve. This is due to a weak upward oriented field emanating from the left-hand slab, as shown in Figure 4.20. An interesting aspect of the tertiary fields in this model series is that the tertiary magnetic field from the left-hand slab is more spread-out than that of the right-hand slab. This is because the tertiary currents are nearly horizontal, and circulate over a wide area on the horizontal plane of the slab. At the region in between the two slabs, the upward tertiary magnetic field from both slabs results in a higher positive peak.

The mutual coupling for the vertical, longer left-hand slab are shown in Figure 4.21. Here there is a strong positive peak at $x \sim 0$, and a smaller positive anomaly at $x \sim$ 12 m. In between the two positive peaks, there is a sharp negative peak at $x \sim 7.5$. There is a sign change in the H_z fields for all three frequencies at x ~ 10. The fields tend to ramp off towards zero at the far end on both sides. The tertiary magnetic field lines emanating from the slabs in this model are also shown in Figure 4.21. Here it is seen that the field lines from left-hand slab are more horizontal than the right-hand slab. The sharp negative peak located at the location of the right-hand slab is due the downward oriented field lines fluxing through the slab.

Figure 4.22 shows the tertiary H_z field for the case when the left-hand slab is a cube. As in the previous models, the H_z field is characterized by a slight offset of the main peak from the x =0 position towards the cube. For the resistive cube, the main peak is positive. There is another positive peak to the right of the main peak, which ramps-off towards zero. In between the two peaks, there is a sharp negative peak above the location of the right-hand slab. A second negative anomaly is present at x ~ -12, which is smoother, and slightly stronger than the negative anomaly on the right-hand side. The tertiary field lines for this model have been presented in Figure 4.22. It is seen that the tertiary field for the left-hand slab is almost that of a vertical magnetic dipole. This is because as the secondary magnetic field lines from the right-hand slab pass through the faces of the cube, most of the field lines pass through the vertical faces, which will induce a set of vertical secondary currents. The cube should then act as a tertiary vertical magnetic dipole; however, a portion of the secondary currents passing through the top of the cube adds a downward component to the tertiary currents. The tertiary magnetic field from the right-hand slab is oriented upwards, and tilted to the left. The sharp negative peak above the right-hand slab is due to the field lines oriented in the z direction.

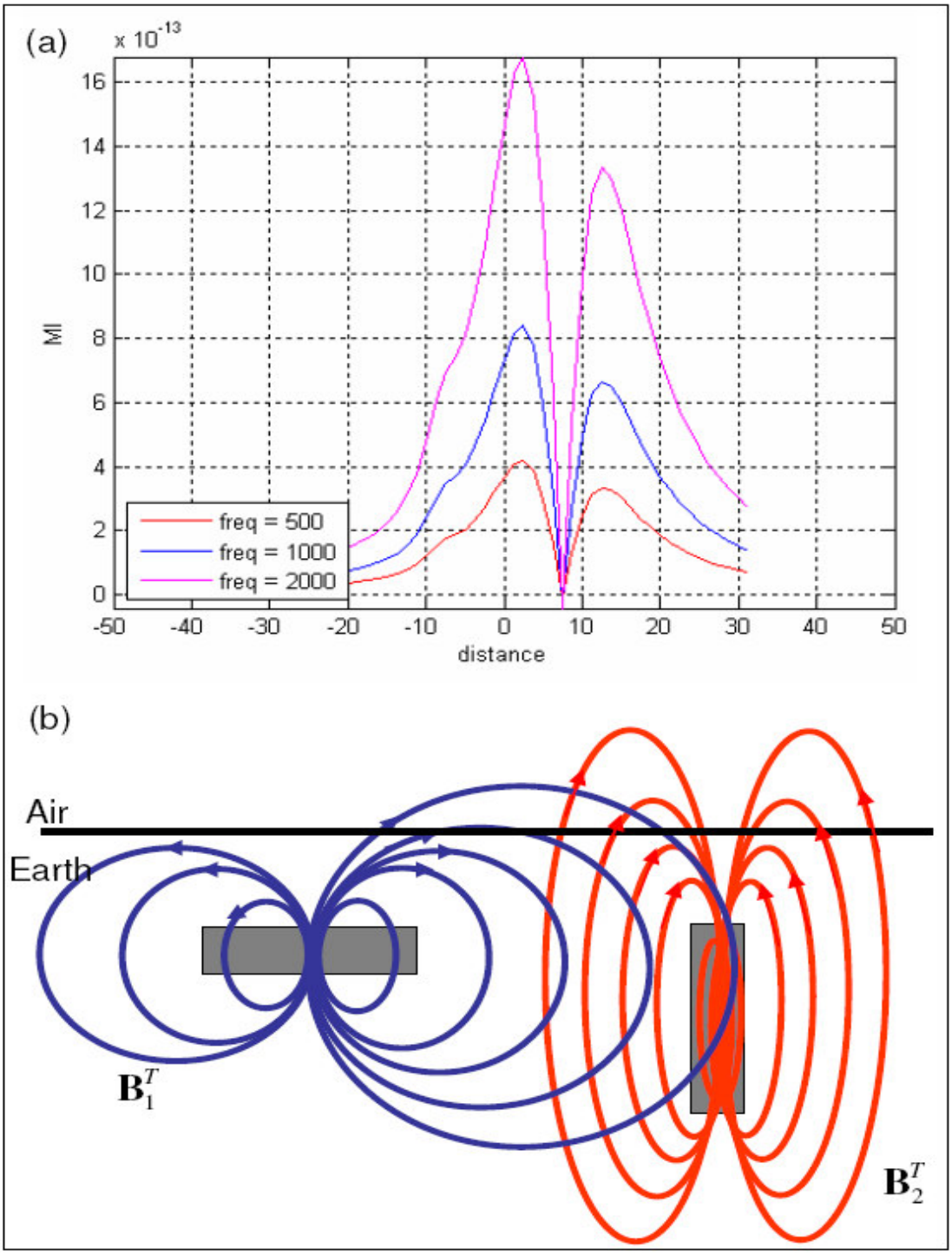

Figure 4.20. Mutual inductance (a) for model suite H, with left-hand horizontal slab and associated tertiary magnetic (b) field lines emanating from slabs.

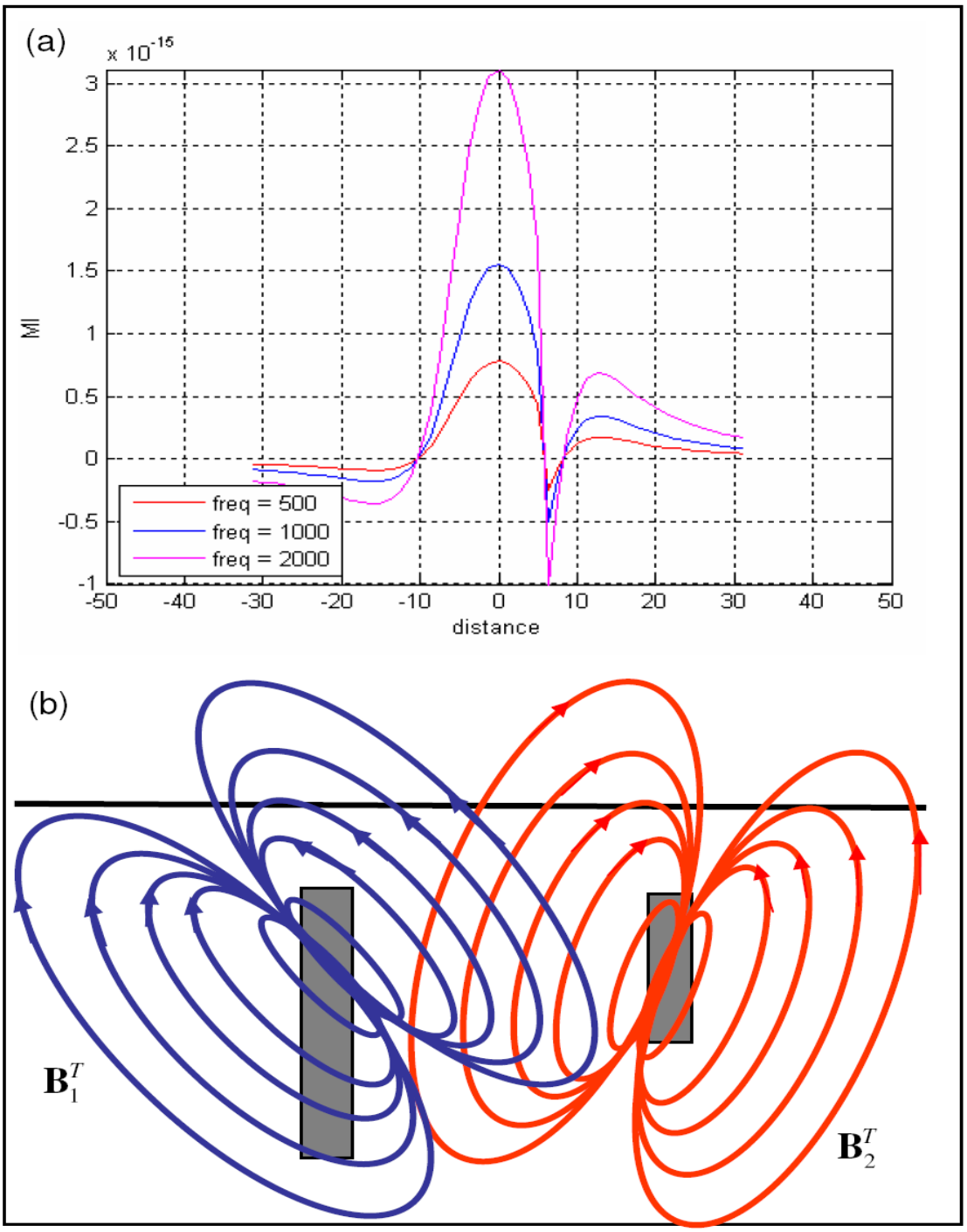

Figure 4.21. Mutual inductance (a) for model suite H, with longer vertical slab and associated tertiary magnetic (b) field lines emanating from slabs.

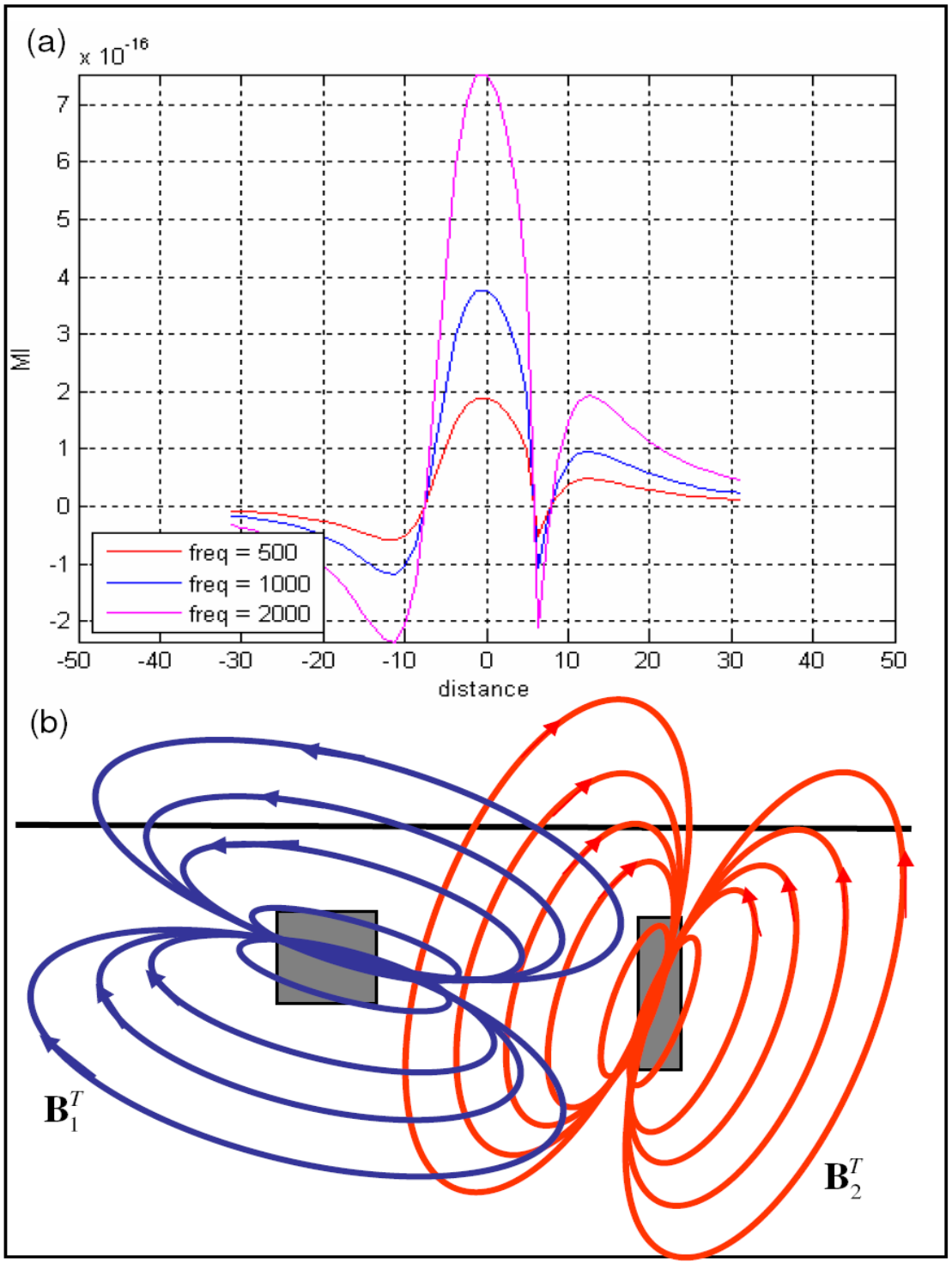

Figure 4.22. Mutual inductance (a) for model suite H, with cubic left-hand slab and associated tertiary magnetic (b) field lines emanating from slabs.

CHAPTER V
SUMMARY AND CONCLUSIONS

The interaction between two buried targets due to mutual inductance was successfully determined for a series of models. This has been analyzed to determine the process involved in determining the orientation and shape of secondary and tertiary currents that contribute to the mutual inductance in buried targets. Some very interesting assessments have been made based on this study.

The host conductivity has a huge role to play in determining the tertiary currents in a target. If the host conductivity is greater than the conductivity of the target, the magnetic field lines emanating from that target will circulate in a direction opposite to the direction followed by the right-hand rule. In the presence of a cultural conductor, a resistive target will give a response that is opposite to that from a conductive target. While it is easier to determine if the heterogeneity is resistive or conductive, determining the actual conductivity of the target is a more difficult task. This is especially true if the target is resistive.

Another important outcome from this study is the one-sided horn that develops over a conductive target when the transmitter is located above another target. This has tremendous potential for application in a profile type survey. If the TX can be placed above a known source of cultural noise, may be possible to determine a conductive heterogeneity in the vicinity of the conductor. This technique will work best in a resistive terrain, such as limestone, which will lead to a strong positive effective conductivity for geological features such as clay or water filled fractures.

In addition to these we see that shape and orientation of the targets plays an important role in determining the magnitude and orientation of the tertiary EM fields. We see that induced currents in a target have a proclivity towards circulating on a surface that has higher area. This may result in a very complicated tertiary field for compact targets, as seen in the case of the cubic left-hand slab.

From the previous chapter of this thesis, it is evident that the interaction between two targets in a CSEM experiment results in a very complicated tertiary magnetic field. In a field experiment, if the source of cultural noise is known, as in the case of a metal fence or railroad tracks, it is possible to model the secondary field from this source and to remove it from the dataset. However, removing the tertiary fields generated by mutual induction is a more complex process. A number of factors must be accounted for when trying to isolate the effect of mutual coupling from a given EM dataset. These include, and are not restricted to, the size, shape, orientation, and conductivity of targets. Even with the most careful and detailed attempts at removing mutual coupling from the dataset, it is very unlikely that all traces of this effect will be removed. The reason I say this is because at a field site, when one is not aware of the location and number of targets in the vicinity of the experiment, on cannot calculate the effect of mutual coupling. It is not possible to give a standard formula to remove the effect of mutual coupling from a dataset simply due to the large number of variables involved in the electromagnetic interaction between two or more targets. Data which is suspected to have an element of cultural noise must be examined closely so as to not be misinterpreted.

As a final thought, it is interesting to look at mutual inductance from a different perspective. So far we have seen how two targets electromagnetically interact with each other in the presence of a primary magnetic field, and this is done with the idea that we want to remove this effect from the field dataset. However, does one really wish to remove these tertiary fields? Consider the case of a field experiment with a known source of cultural noise. Here the metal conductor will act as a source of secondary currents and will only increase the response from buried geological targets. Perhaps, this mutual inductance need not be ‘noise’ in the dataset, but an extra tool to help identify the unknown targets. There is much potential for the use of mutual inductance between cultural noise and a target as an aid in geological interpretation of CSEM field data, and I feel that further study of this field will only increase the utility of MI in CSEM exploration, especially for near-surface experiments.

REFERENCES

Badea, E., M. Everett, G. Newman, and O. Biro, 2001, Finite-element analysis of controlled-source electromagnetic induction using Coulomb-gauged potentials: Geophysics, **66**, 786-799.

Biro,O., and Preis, K., 1989,On the use of the magnetic vector potential in the finite element analysis of three-dimensional eddy currents: IEEE Trans. Magn., **25**, 3145–3159.

Collins, E.W., 1987, Characterization of fractures in limestones, northern segment of the Edwards aquifer and Balcones fault zone, central Texas: GCAGS transactions, **37**, 43-54.

Collins, E.W., 1995, Structural framework of the Edwards aquifer, Balcones fault zone, central Texas: GCAGS Transactions, **45**, 135-142.

Collins, J.L., Everett M.E., Johnson C.B., 2006, Detection of near-surface horizontal anisotropy in a weathered metamorphic schist by transient electromagnetic induction: Phys Earth Planet Inter **158** 159-173.

Constable, S.C., Parker, R.L., Constable, C.G., 1987, Occam's inversion: A practical algorithm for generating smooth models from electromagnetic sounding data: Geophysics, **52**, 289–300.

Everett, M.E., 2007, Class notes, Geop 413 – Near surface geophysics, Texas A&M University, College Station.

Everett, M.E., Shultz, A., 1996, Geomagnetic induction in a heterogeneous sphere: Azimuthally symmetric test computations and the response of an undulating 660-km discontinuity: Journal of Geophysical Research, **101**, 2765-2783.

Ferrill D.A. , Sims, D.W., Waiting, D.J, Morris, A.P, Franklin, N.M., Schultz, A.L. 2004, Structural framework of the Edwards Aquifer recharge zone in south-central Texas: GSA Bulletin; **116**, (3-4), 407-418.

Fitterman, D.V., Labson V.F., 2005, Electromagnetic induction methods for environmental problems, in near surface geophysics, SEG, Investigations in Geophysics, **13**, 301-357.

Mancini, E.A., and Scott, R.W., 2006, Sequence stratigraphy of Comanchean Cretaceous outcrop strata of Northest and South-Central Texas: Implications for enhanced petroleum exploration: GCAGS Transactions, **56**, 539-550.

McNeill, J.D., 1980, Application of transient electromagnetic techniques: Geonics Limited Technical Note, TN-7.

Purcell, E.M., 1965, Electricity and magnetism, Berkeley physics course, **2,** 246 – 249.

Qian, W., Boerner, D. E., 1994, Electromagnetic response of a discretely grounded circuit – An integral equation solution: Geophysics, **59**, 1680-1694.

Qian, W., Boerner, D. E., 1995, Electromagnetic modelling of buried line conductors using an integral equation: Geophysics, **121**, 203–214.

Sasaki, Y., 2001., Full 3-D inversion of electromagnetic data on PC: J. Appl.Geophys., **46**, 45–54.

Sasaki, Y., Meju M.A., 2006, A multidimensional horizontal-loop controlled-source electromagnetic inversion method and its use to characterize heterogeneity in aquiferous fractured crystalline rocks: Geophys. J . Int, **166**, 59-66.

Skinner D., Heinson, G., 2004, A comparison of electrical and electromagnetic methods for the detection of hydraulic pathways in a fractured rock aquifer, Clare valley, South Australia: Hydrogeology Journal **12**, 576-590.

Stalnaker, J., 2004, A finite element approach to the 3D CSEM modeling problem and applications to the study of the effect of target interaction and topography. PhD Dissertation, Department of Geology and Geophysics, Texas A&M University.

Stalnaker, J.L., Everett, M.E, Benavides, A., Pierce, C.J., 2006 Mutual induction and the effect of host conductivity on the EM induction response of buried plate targets using 3-D finite element analysis: IEEE.Trans Geosci. Remote Sens. **44**, 251-259.

Taucer, P., 2006 The effects of Juniper removal on rainfall partitioning in the Edwards Aquifer region: large-scale rainfall simulation experiments: MS Thesis , Department of Agricultural Engineering, Texas A&M University.

VITA

Roland Anthony Savio Fernandes
Email: rolyfernandes@tamu.edu
Address: Dept of Geology and Geophysics, M.T. Halbouty Building,
TAMU, College Station, TX 77843-3115

EDUCATION

Texas A&M University, College Station, TX.
M.S. in Geophysics, May 2008.

University of Pune, Pune, India.
M.S. in Geology, May 2005.

University of Mumbai, Mumbai, India.
B.S. in Geology, May 2003.